MASTERARBEIT / MASTER'S THESIS

Titel der Masterarbeit / Title of the Master's Thesis

„Group-delay charactization of MID-IR mirrors via white-light interferometry "

verfasst von / submitted by

Laurin Steidle, BSc

angestrebter akademischer Grad / in partial fulfilment of the requirements for the degree of

Master of Science (MSc)

Wien, 2019/ Vienna, 2019

Studienkennzahl lt. Studienblatt / degree programme code as it appears on the student record sheet:	A 066 876
Studienrichtung lt. Studienblatt / degree programme as it appears on the student record sheet:	Masterstudium Physik / Master's degree programme Physics
Betreut von / Supervisor:	Dr. Oliver Heckl

Abstract

Precise dispersion control is indispensable for ultrafast optical devices and broad bandwidth enhancement cavities. In the framework of this thesis, an instrument to measure the dispersion of mirrors and other optics is built and analyzed. We use a Michelson-type interferometer and a broadband white-light source that extends into the mid-IR (up to 5 μm). We achieve a resolution of below 1 nm and a standard measurement error of below 10 fs^2. Sources of error have been rigorously analyzed and, if possible, eliminated. The measurement instrument will serve as a long-term diagnostic tool for the development of crystalline mirror coatings, ultra-fast mid-IR light sources and mid-IR enhancement-cavities.

Zusammenfassung

Präzise Dispersionkontrolle ist unverzichtbar für ultraschnelle optische Geräte und breitbandige Enhancement-Cavities. Im Rahmen dieser Arbeit wird ein Instrument zur Messung der Dispersion von Spiegeln und anderen optischen Elementen gebaut und analysiert. Wir benutzen ein Michelson-Typ Interferometer und eine breitbandige Weißlichtquelle die bis in den mittleren Infrarot (bis zu 5 μm) reicht. Wir erreichen eine Auflösung von unter 1 nm und einen Standardmessfehler von unter 10 fs^2. Fehlerquellen wurden ausführlich untersucht und wenn möglich verbessert. Das Messinstrument wird als ein dauerhaftes Mess- und Diagnosewerkzeug für die Entwicklung von kristallinen Spiegeloberflächen, ultraschnellen mittleren Infrarotlichtquellen und Enhancement-Cavities verwendet.

Inhaltsverzeichnis

1 Introduction

Background In June of 2017 the Christian-Doppler-Labor for Mid-IR Spectroscopy and Semiconductor Optics (CDL-MIR) was officially opened. The Christian Doppler Research Association promotes the cooperation between scientific research groups and industry. In case of the CDL-MIR a cooperation with Crystalline Mirror Solutions (CMS) was initiated. CMS is a manufacturer of low Brownian-noise, highly reflective optics using a novel crystalline coating technology. It was founded as a spin-off of fundamental physics research at the University of Vienna by Dr. Garrett Cole and Dr. Markus Aspelmeyer.

As part of the cooperation with CMS, the CDL-MIR provides diagnostic tools for their products. One of them is a dispersion measurement setup, which will be discussed in the following thesis.

Aim The Aim of this work is to build a setup that is able to accurately measure dispersion of mirrors and other optical components in the mid-infrared regime over a wide wavelength range. The measurement setup is used for the characterization of crystalline mirror coatings. It is required that all possible sources of errors are well understood and if possible minimized.

As a first prototype we build the measurement instrument in the visible regime. We chose a visible regime, because similar instruments have been shown to work in that spectral region. Also because optical components are significantly cheaper and alignment is much easier in that spectral region as one is able to see the light by eye. Unexpected problems can be identified and technical constraints such as requirements for i.e. electronics can be thought through and tested thoroughly.

In the next phase we translate the setup into the mid-infra red (MIR) regime. After reproducing all functions and recording characterization measurements the quality of these results is examined. We carry out a thorough examination of all error sources found and implement or suggest improvements until all requirements are fulfilled.

2 Theoretical Background

This chapter will be a short introduction to all theoretical concepts necessary for understanding the thesis.

2.1 Chromatic Dispersion

Chromatic Dispersion describes the dependence of the phase velocity of light on the wavelength. This effect can be caused by a wavelength dependent refractive index of an optical medium. A famous example of this effect is a prism that splits white light into its spectrum. However, the effects of dispersion are not limited to this and do not need to change the propagation path for different wavelengths. To get a better understanding of the many effects of dispersion, we will examine the effect of a dispersive media on a light pulse.

A light pulse always consists of several wavelengths due to its finite length even if the carrier wave is monochromatic. Therefore, the spectrum of a light pulse is always extended over a certain spectral region. In figure 2.1 an exemplary light pulse and its spectrum is shown.

If we assume the light pulse propagated through a medium in which all spectral components have the same phase velocity, a constant phase will be added to the light pulse over its full spectrum. This additional constant phase causes a phase shift of the carrier wave. However, the pulse envelope and its centroid remain the same. When the light pulse propagates through a dispersive medium the phase added to the pulse is non-constant relative to the wavelength. If this dependency is linear, the pulse envelope will be shifted while the carrier wave still has the same phase relative to the centroid of the pulse. When the phase velocity has a non-linear dependence on the wavelength (i.e. of second order), the pulse envelope will be stretched or squeezed. Additionally, the carrier frequency of the original pulse will be chirped. Higher order dispersion changes the pulse shape and distort the carrier frequency, but is often weak compared to the effect of the second order dispersion. All these processes are linear in the sense that the combination of several orders of dispersion i.e. linear and quadratic, result in the superposition of these effects.

Due to these effects, dispersion is a crucial quantity to be controlled when working with pulsed light systems.

We will now formalize the concepts introduced the in the previous section. For reference see [1]. Chromatic dispersion is defined by the Taylor expansion of the wavenumber $k = \frac{2\pi}{\lambda}$ with respect to variations in spectral phase. For reference, see [2].

$$k(\omega) = k\left(\omega_0\right) + \frac{\partial k}{\partial \omega}\left(\omega - \omega_0\right) + \frac{1}{2!}\frac{\partial^2 k}{\partial \omega^2}\left(\omega - \omega_0\right)^2 + \frac{1}{3!}\frac{\partial^3 k}{\partial \omega^3}\left(\omega - \omega_0\right)^3 + O^4 \tag{2.1}$$

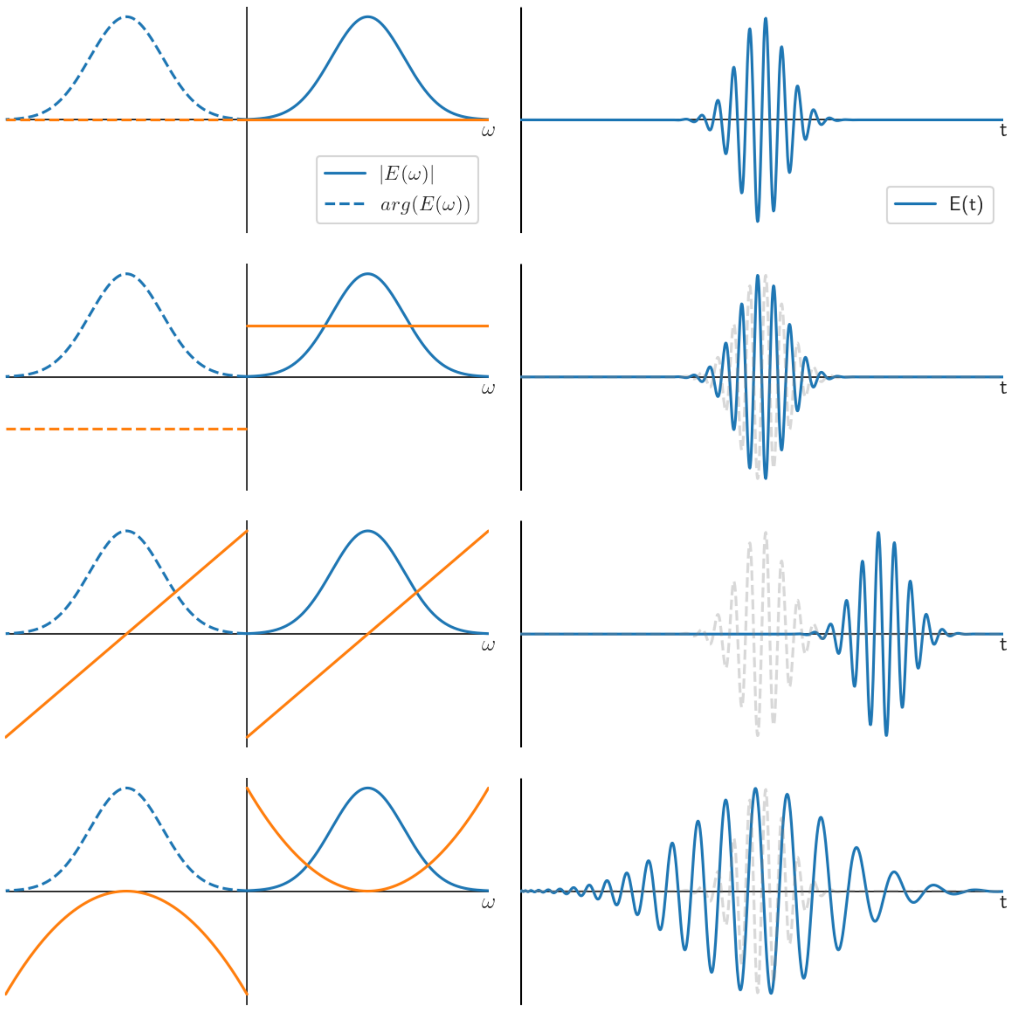

Abbildung 2.1: The different rows show the effect of different order of dispersion. In the left column the spectrum and phase of a particular signal is shown. The phase is shown in orange while the spectrum is shown in blue. The dashed lines show the imaginary part, while the solid lines show the real part. On the right side the resulting light pulse is shown. The original pulse is shown as a dashed line.

The first term represents a common phase shift, leaving the pulse shape and position untouched. The first-order term can also be expressed in terms of the inverse group velocity and is therefore responsible for an overall time delay of the pulse, while still leaving the pulse shape untouched. The second order term or quadratic term is commonly called the group delay dispersion or short GDD.

$$k'' = \frac{\partial^2 k}{\partial \omega^2} \tag{2.2}$$

We will mainly focus on the GDD as its understanding is critical in many applications due to its influence on the pulse shape. It is most commonly expressed in units of fs^2 or alternatively in seconds per meter.

3 Experimental Setup

3.1 Working Principle

The task of this setup is to measure chromatic dispersion of mirrors or other optical components. A similar setup has been presented by Diddams et al. for the visible regime [2]. In general, this setup can be used to determine the dispersion of all kinds of optical components that can be integrated into the interferometer. However, we are interested in mirrors and will therefore focus our discussion almost exclusively on them, well aware of the fact that other applications are also possible.

To determine the dispersion of a mirror we compare it to a reference mirror. If the dispersion of the reference is well known, the dispersion of the sample mirror is the difference between the dispersion of the reference mirror and the measured dispersion. This is of course easiest if the reference mirror is not dispersive. In that case the measured dispersion is equal to the dispersion of the sample mirror. For this reason we will be using metal coated mirrors as a reference because their dispersion is vanishing for all wavelengths of interest. We can compare the relative phase shift of two mirrors on the same incoming wave with a Michelson interferometer. The incoming light is split up by a beam splitter into two arms of the interferometer. Both reflected light beams are then recombined in the same beam splitter where the resulting wave is a superposition of the reflected light of both arms. By placing the sample mirror in one arm and a metallic mirror in the other, we are able to measure the dispersion of a sample mirror. A schematic of the described setup is shown in figure 3.1. This kind of setup, which uses a broad-band light source, is commonly referred to as 'white-light-interferometer' (WLI).

However, we are not able to directly measure the dispersion. We rather capture the interference pattern created in the Michelson-Interferometer when scanning through the relative path lengths of the interferometer arms. The simplest way to do this is by mounting one arm of the interferometer on a translation stage. The stage can be moved while measuring the intensity of the interferometer output. This creates a changing optical path difference (OPD) between the two arms of the interferometer and a changing interference pattern. An exemplary detector signal resulting from a coherent monochromatic source is shown in figure 3.2.

In case of a broad-band source, we have a much more complex shape of the interferogram created by the super-position of all present wavelengths. Because the coherence length of broad-band sources is short, the broad-band interferogram is only a short burst. The exact shape of this burst is determined by the spectrum and phase of the light source. An exemplary burst of a broad-band light source is shown in figure 3.3.

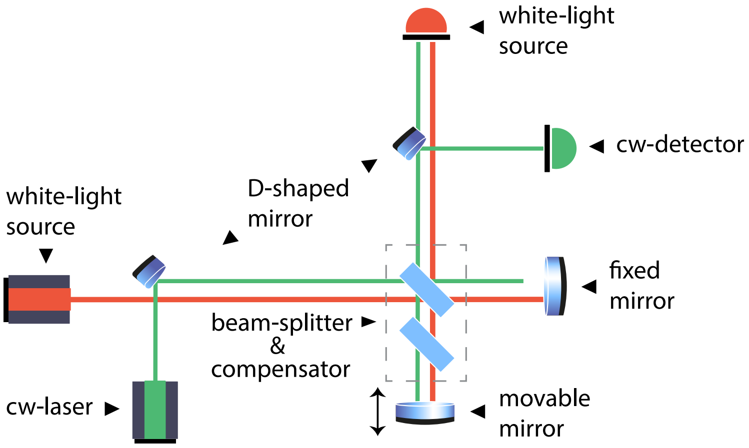

Abbildung 3.1: Conceptual setup design. Calibration laser is coupled onto the same beam path. The interferograms of both light sources can be recorded by moving the bottom mirror parallel to the beam path.

The fringe pattern recorded by the described procedure can be expressed as

$$I \propto \left\langle |E_1(t) + E_2(t+\tau)|^2 \right\rangle \tag{3.1}$$

where E represents the field amplitude from mirror one and two respectively and τ describes the delay between the two fields created by changing the distance between mirror two and the beam splitter. This equation can be rewritten into

$$I \propto \left\langle |E_1(t)|^2 \right\rangle + \left\langle |E_2(t)|^2 \right\rangle + \underbrace{\langle E_1(t)E_2^*(t+\tau)\rangle \cdot exp(-i\omega\tau) + \langle E_1^*(t)E_2(t+\tau)\rangle \cdot exp(i\omega\tau)}_{=:A} \tag{3.2}$$

The third term of the last equation carries all the important information, because $\left\langle |E_2(t)|^1 \right\rangle$ and $\left\langle |E_2(t)|^2 \right\rangle$ are constant. We therefore neglect the constant terms and only focus on the last term. We will now examin the fourier transformation of this term. Because it is real valued if follows that the Fourier transform will contain two equal positiv and negativ frequency parts.

$$A^+ = \langle E_1^*(t)E_2(t-\tau)\rangle \cdot exp(i\omega\tau) \quad or \quad A^- = \langle E_1(t)E_2^*(t-\tau)\rangle \cdot exp(-i\omega\tau) \tag{3.3}$$

We can neglect A^- because it contains the same information as A^+. Through the Fourier transformation of A^+ we receive:

$$FT(A^+) = E_1(\omega)^* \cdot E_2(\omega) \tag{3.4}$$

Conceptionally, E_1 and E_2 differ only by a relative phase. Therefore, we can express E_2 by

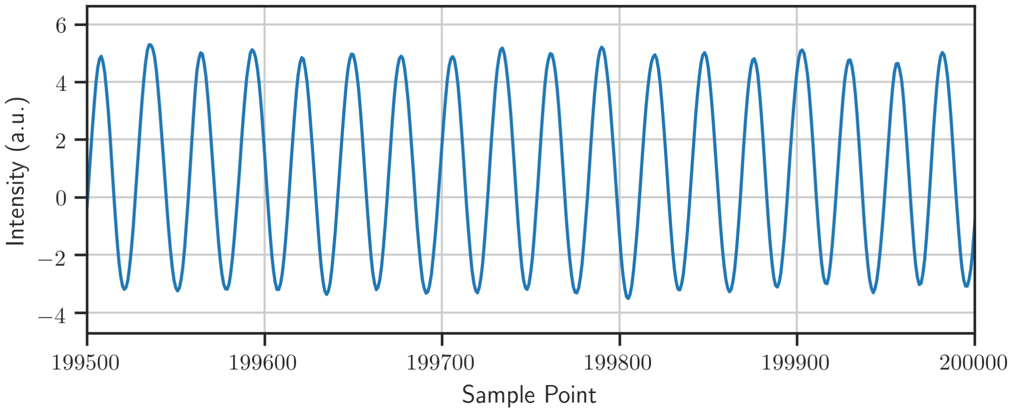

Abbildung 3.2: Exemplary calibration laser interferogram recorded by moving one arm of the interferometer with constant velocity.

E_1 times an additional phase term r_{12}:

$$FT(A^+) = E_1(\omega)^* \cdot E_2(\omega) \tag{3.5}$$

$$= E_1(\omega)^* \cdot r_{12}(\omega)E_1(\omega) \tag{3.6}$$

$$= r_{12}(\omega)|E(\omega)^2| \tag{3.7}$$

r_{12} is a complex, frequency dependent function. While it can be used to also represent amplitude differences, we will focus on phase shifts in the two arms of the interferometer. The last equation can then be used to calculate the phase of the recorded signal. It is given by the angle between the complex and and real part of $FT(A^+)$

A similar process is used in Fourier-transform infra-red spectroscopy (FTIR) which is widely used and a well known measurement technique. In this case however, both interferometer arms are identical since the sample is placed outside of the interferometer. This results in equation 3.4 transforming into

$$FT(A) \propto E(\omega)^* \cdot E(\omega) = |E(\omega)|^2 \tag{3.8}$$

Therefore, only the spectral information can be extracted and the effect on the phase remains unknown. A schematic representation of the difference between these two setup types is shown in figure 3.4.

A WLI uses a broad-band light source. It offers the benefit of being able to measure a broad spectral range simultaneously. This does not only make it possible to measure a variety of different components with the same light source, but is also necessary because we need to derive the phase with regard to its wavelength to receive the GDD. The captured signal is evaluated in a Fourier analysis as described above and the phase can be calculated for every

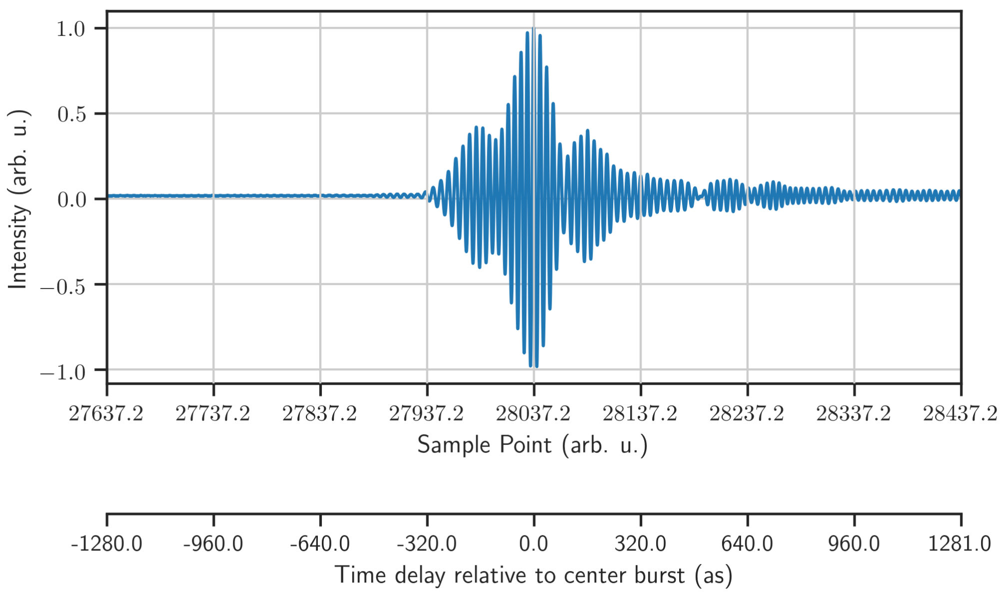

Abbildung 3.3: Interference burst of an exemplary broad-band light source. Take note on the short interference length.

wavelength present in the signal. A detailed description how this is done can be found in section 4.2. When the captured signal is Fourier transformed, the phase extracted represents the relative phase of the reflected light beams from the reference and sample mirror. The second derivative of the mirror-induced phase shift, with respect to its wavelength, is the GDD of the sample mirror. In general, one could obtain any order of dispersion with the same principle. However, we mainly focus on the GDD.

We are measuring the interferogram by changing the OPD between the two interferometer arms and are therefore sampling our signal as a function of the translation stage position. This introduces two ambiguities:

The first one is that for a Fourier-transform we need to guarantee that all sample points are equally spaced. This assumption can of course be easily violated, as it would require us to determine the position of the stage with a sub nm precision. The second one is that we lose the natural frequency axis for our Fourier transform because we are not sampling our interferogram as a function of time but rather as a function of stage position. Therefore, we need a way to recalibrate this axis.

Both ambiguities can be resolved by also capturing an interferogram of a coherent spectrally narrow source, where the central frequency is well known. To consistently distinguish the two signals, we captured them with two different detectors. The reference laser is set

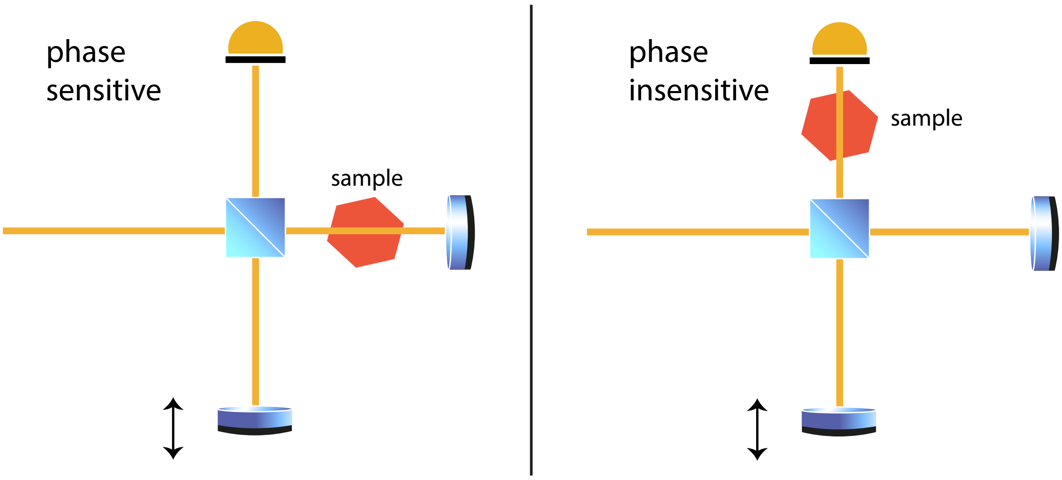

Abbildung 3.4: On the left a phase sensitive configuration is shown as described before while on the right a phase unsensitive setup is shown. The key difference is that the sample is placed in one of the interferometer arms in case of the phase sensitive setup.. A phase unsensitive setup places its sample outside the interferometer. This obscures the phase information in the measuring process.

up such that its optical axis has a parallel offset to the white-light band beam while still staying in the same beam path. The laser beam is then picked up by a D-shaped mirror and diverted onto its detector.

This reference interferogram carries two important pieces of information. The first one is its phase at every sample point. Due to the precise knowledge of the phase of the reference, we also know the distance between two sample points with high precision. This knowledge can then be used to recalibrate our measurement and therefore guarantee that all sample points are equally spaced. This resolves the first ambiguity. The second information we receive from the reference interferogram is its frequency. Because frequency of the reference laser is well known, we can use it to calibrate the frequency axis of the Fourier transformation, resolving the last ambiguity. Further details on this can be found in section 8.1.

The downside of any broad-band source is that it either has short coherence length in case of an incoherent source or it has a short pulse duration in the case of a coherent source. In the case of our incoherent light source, its coherence length is roughly 100 μm. In principle, this makes alignment extremely difficult because the interference pattern is only visible in this short range. However, this problem can be avoided by using the reference laser to align the interferometer. The alignment process for the reference laser is very easy due to the large coherence length compared to our path length and its small spot size. We use a visible wavelength for our reference. Therefore, everything can be aligned by eye without the need for any additional tools. Because the reference beam is propagating through the same interferometer, we automatically align the beam path of the broad-band source when aligning it for the reference laser. The only free parameter after aligning the setup with the reference is the stage position of the center burst, which can be found by simply scanning through the travel range of the stage.

Now that we understand how the setup functions we will discuss how the data is recorded. The digitization of a signal always introduces an error due to the limited amount of discretization levels. The detector signal needs to be well conditioned before capturing it with an analog-digital-converter (ADC) to minimize this error. The key aspect for this problem is to condition the signal in such a way that the full dynamic range of our ADC can be used. This is especially important because different sample mirrors vary strongly in their reflectivity, center wavelength and size. Hence, the signal intensity will vary strongly and has to be adjusted to minimize discretization errors. This is done by a home build adjustable amplifier (see section 3.5).

To capture the voltage from the detector, a simple data acquisition card (DAQ) (see section 3.4) is used. The DAQ is configured to write the measurement data in a continuous stream onto a control computer. The evaluation of this file will be discussed in section 4.2.

The full setup in its final configuration can be seen in 3.5 and 3.6. The setup is basically doubled to extend its effective spectral range. The first interferometer covers the near-IR spectral region (NIR) starting from 500 nm up to 1000 nm, while the second interferometer covers the mid-IR (MIR) from 1 μm to 5 μm. Conceptually, there is no difference in between these two interferometers. Due to limitations of optical components they are split in two. As one can see, both NIR and MIR setups are combined to reduce the space and parts needed.

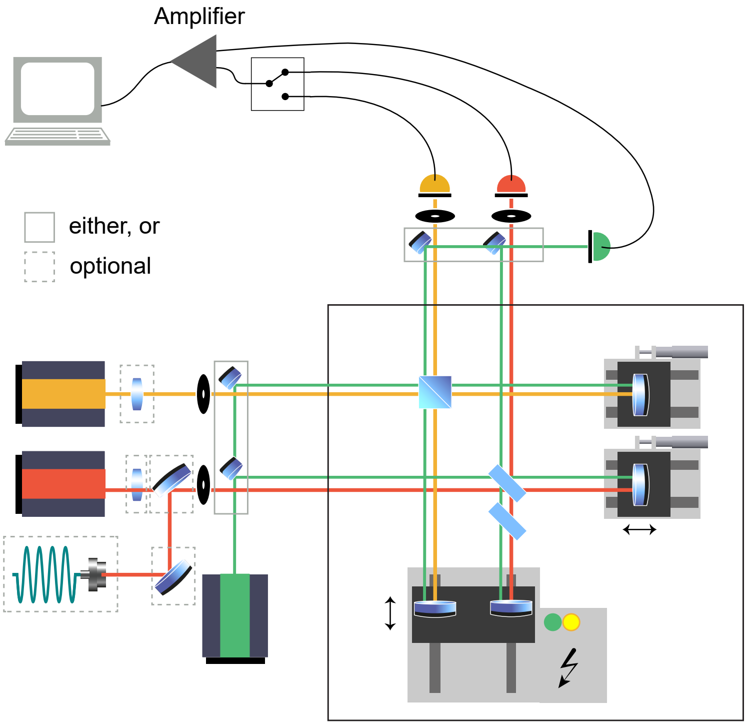

Abbildung 3.5: Schematic setup of the doubled Michelson interferometer. Both interferometers are combined to reduce size and the amount of components. The calibration laser beam path has a slight offset so it can be picked up with a D-shaped mirror and projected onto a separate detector. The lower interferometer arm gets delayed to capture the interferometer.

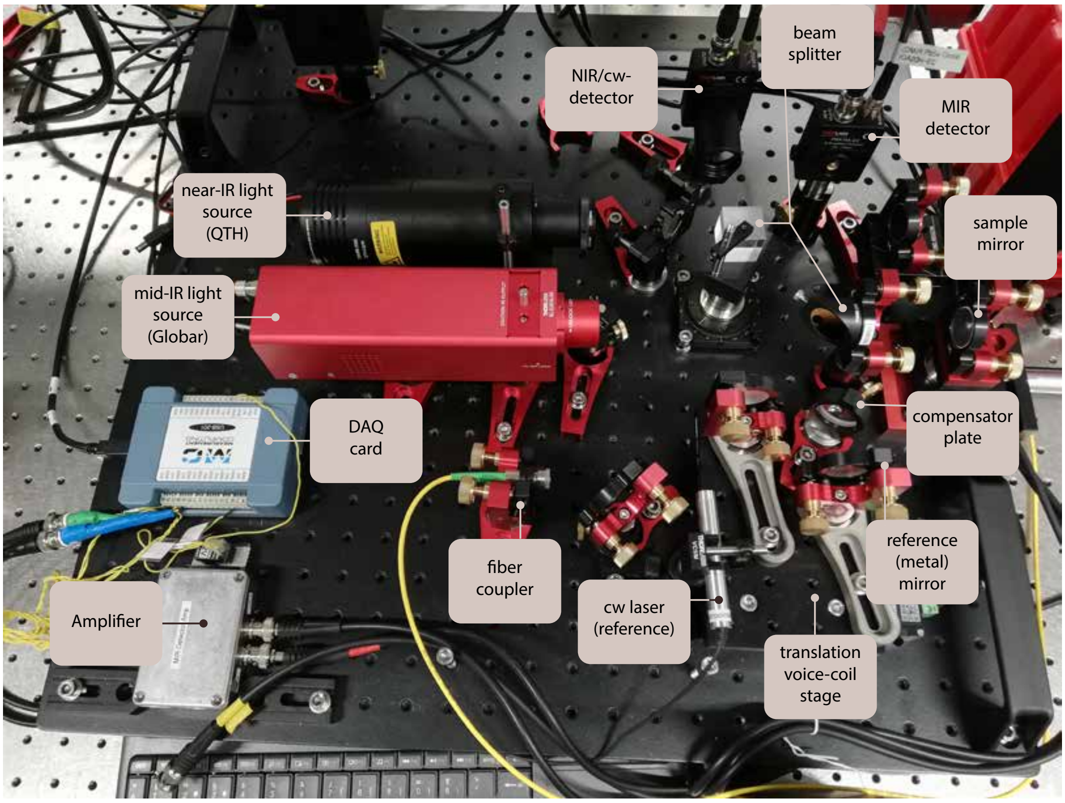

Abbildung 3.6: Picture of the current setup as schematically shown in figure 3.5

.

3.2 Wavelength Resolution Limits

One crucial aspect for any FTS is its resolution. The formula for wavelength resolution limit $\Delta\lambda$ of a white light interferometer (WLI) can be derived easily from the relation between frequency and wavenumber. It is given by

$$f = c\,\widetilde{\nu} \tag{3.9}$$

where f represents frequency, $\widetilde{\nu}$ the wavenumber and c is the speed of light. To examine the effect of variations, one calculates the differential of the previous equation.

$$df = c\,d\widetilde{\nu} \tag{3.10}$$

$$\Delta f = c\,\Delta\widetilde{\nu} \tag{3.11}$$

If we solve this equation for $\Delta\widetilde{\nu}$ one notices that it takes the form of a distance. This distance represents the maximal optical path difference (OPD) between the two interferometer arms. Hence, we end up with:

$$\Delta\widetilde{\nu} = \frac{1}{OPD} \tag{3.12}$$

In our setup, the maximal distance that one arm can get extended or shortened represents only half the OPD since the light needs to travel this distance twice.

While wavenumbers are a common unit used in spectroscopy, one might find it more intuitive to think about it in terms of wavelengths. To do this, we start with the relation between wavenumbers and wavelengths and go through the same process.

$$\widetilde{\nu} = \frac{1}{\lambda} \tag{3.13}$$

$$\Delta\widetilde{\nu} = \frac{1}{\lambda^2}\Delta\lambda \tag{3.14}$$

$$\Rightarrow \Delta\lambda = \frac{\lambda^2}{OPD} \tag{3.15}$$

Note that this introduces a quadratic wavelength dependence into the wavelength resolution. Hence, with the same OPD one achieves different resolutions at different wavelengths. The wavelength resolution differs drastically depending on which wavelength you wish to resolve. For example: at a wavelength of 1030 nm, we achieve a resolution of 0.05 nm with a delay of 10 mm. For the same delay, at a wavelength of 3000 nm, we end up with a resolution of 0.4 nm. At the upper frequency limit of 5000 nm we merely have a resolution of 1 nm.

In general, it is possible to increase the delay between two arms until a desired resolution is achieved. However, for larger delays several new sources of error occur. The main problems in our case were the collimation of the light source and unwanted reflections in the setup. This prevents us from easily increasing the maximal OPD.

Another common limiting factor are back-reflections. Our setup is required to work for a broad range of wavelengths which make anti-reflection coatings unpractical. An unfortunate effect of this is the presence of strong unwanted reflection at optical components that can be clearly visible in the interferogram.

The incoming light wave traverses an optical component. On the 'back' boundary layer, when the wave is exiting the medium, a small portion will be reflected. The reflected part of the wave goes through the same process while traveling in the opposite direction and is reflected again on the 'front' boundary of the medium. This creates a delayed copy of the original wave with the same propagation direction, but only if both incident boundaries are parallel to each other. Such back-reflections are visible in the interferogram as 'side bursts'.

These side bursts create distortions in the measured spectrum and phase. Therefore, limited the interferometer so that side burst can be avoided. This can be done by using optical components that cause an extra optical path length for reflections that is higher then the OPD, or by limiting the OPD so that side bursts are excluded. Another option to avoid side bursts is to use wedged optics. This way the back reflection is not projected away from the detector. However, this is only possible for optical components which are not to close to the detector. Otherwise the necessary wedge angle can become unpractical.

So far, we discussed the physical wavelength resolution limitations based on the OPD of our interferometer. While equation 3.13 represents a physical lower frequency resolution constraint, there is also a limit for the maximal frequency detectable in the input signal, given by the Nyquist frequency,

$$f_{Nyquist} = \frac{f_s}{2} \tag{3.16}$$

with f_s being the sampling frequency in Fourier time domain. Equation 3.16 transforms to a lower wavelength bound frequency limit of

$$\lambda_{min} = \lambda_{Nyquist} = 2 \cdot \Delta x \qquad \text{or} \qquad \Delta x = \frac{\lambda_{min}}{2} \tag{3.17}$$

where Δx represents the distance between sample points.

During a measurement we do not directly sample the interferogram as a function of time but rather as a function of OPD. The OPD is a function of the sampling frequency f_s and the velocity of the translation stage v. We need to to chose the sampling frequency in such a way that the desired lower frequency can be resolved according to equation 3.16. The distance between sample points based on the sample frequency and the stage velocity is given by:

$$\Delta x = \frac{v}{f_s} \tag{3.18}$$

In principle, v and f_s can take arbitrary values. However, together with the OPD they actually are the limiting factors in our setup due to technical constraints. Depending on the choice of v and f_s, we end up with the total time that a measurement takes.

$$T = \frac{OPD}{2v}$$

Theoretically, the measurement time is of no particular interest. Nevertheless, it is desirable that the time is as short as possible. It becomes important because certain parameters, i.e.

color temperature, might change over time. This can cause the measurement to be distorted, if the measurement time becomes too long.

3.3 Translation Stage

A crucial component in a moving interferometer design is the translation stage. Especially its angular stability is of importance when used in FTIR's or other moving interferometer designs. Common automated translation stages usually use mechanical gears to translate the rotation of an electric motor into a translation motion. These gears then introduce vibration into the system which cause angular disturbances on the stage. This introduces angular disturbances on the interferometer mirror and disturbs our measurements. To avoid that problem we do not use a mechanical translation stage, which uses gears, but rather a voice-coil stage. Due to the absence of any mechanical parts besides the voice-coil, voice-coil stages introduce only very low power vibrations and angular disturbances by design. The stage can be set to move with constant velocity or oscillate with a fixed frequency during which the interferogram is recorded.

3.4 Data-Aquisition Card

To capture the detector outputs we use a 'Measurement & Computing USB-201' unit. Different kinds of capture cards differ in sampling rate, bit depth, and whether they sample their channels simultaneously or alternating.

For our application we require at least two analog inputs. One is used to capture the signal transmitted from the IR detector. The second channel is used to capture the reference laser. In general we would wish for simultaneous sampling, as it enables us to completely compensate all disturbances in the IR signal, that are also present in the reference signal. However, due to the high amount of oversampling that we are able to use, the frequencies of interest are low compared to our sampling frequency. This causes disturbances in the frequency range of interest to be sufficiently suppressed. Additionally, we found disturbances in the OPD to be exclusively present in frequency ranges below 2500 kHz. For these reasons, we found that we are able to sufficiently compensate our measurement for potential OPD disturbances without simultaneous sampling of both channels. Because simultaneous sampling cards are usually significantly more expensive, we chose to go without this feature.

Another very important characteristic of the DAC card, besides its sampling rate, is its bit depth. The bit-depth n in combination with a voltage input range U defines the distance between discretization levels. The distance ΔU between discretization levels is simply given by:

$$\Delta U = \frac{U}{2^n} \tag{3.19}$$

For a 12-bit DAQ unit and an input voltage range of ± 10 volt, this results in a voltage resolution of approximately 5 mV. This effectively creates a non-Gaussian noise source which we will discuss more detailed in section 5.1.

As introduced in section 2.1, we are interested in the second derivative of the phase. This means, the signal has to be derived twice times depending on the order of dispersion which is of interest. However, numerical differentiation is very sensitive to errors and acts as an error amplifier. Therefore, the relatively low discretization noise is clearly visible as a contributing error source and needs to be minimized if possible.

3.5 Amplifier

During the first tests with the prototype it became clear that we needed some way to amplify the signal output of our detector. The DAQ card we use has a range from -10 to 10 volt. However, the detector output ranges from 0 to 10 volt. If we do not compensate the differences in voltage range, we would have the same discretisation levels spread over half the voltage range. This is equivalent to losing half the resolution which results in the loss of one bit. The current DAQ card only supports 12-bit in resolution, which already results in discretization levels of 5 mV. We will show in section 5 that this will not only be visible in the final result but also be a significant error source.

Furthermore, the setup is by design able to run with different sets of mirrors. These mirrors will have a strong effect on the maximal intensity measured by the detector. Therefore, different levels of intensity will always persist in the experiment and need to be compensated for, if one wishes to decrease the level of noise in the measurement. For these reasons we need to apply some signal conditioning to exploit the full dynamic range of the DAQ card, while leaving a small safety margin to avoid signal clipping.

It would also be possible to simply use a DAQ with a resolution high enough, so that the discretization errors are negligible. However, DAQ cards prices grow rapidly with higher bit-depth. Therefore, we decided to build a simple amplifier which needs to amplify the signal up to ± 10 volt. It also needs to be able to shift the baseline of the voltage. The circuit diagram and other details regarding the amplifier are presented in 3.5.

3.6 Frequency Calibration

The frequency calibration of the signal with the calibration laser is based on the assumption that both beams have the same optical path difference (OPD). However, this assumption can be violated under certain conditions. The OPD differs for the two beam paths if they propagate not parallel but with an angle to each other.

Assume that the signal beam is perfectly aligned. It hits both interferometer mirrors perfectly orthogonal to its surface. If the calibration laser has a slight angle relative to the signal beam, it will also hit the mirrors under the same angle relative to its surface normal. This is shown in figure 3.7.

As a result of this, the calibration laser beam needs to travel a longer distance if one interferometer arm is delayed. This reference OPD (OPD') is related to the perfectly aligned signal OPD by

$$OPD' = OPD \cdot cos(\alpha) \tag{3.20}$$

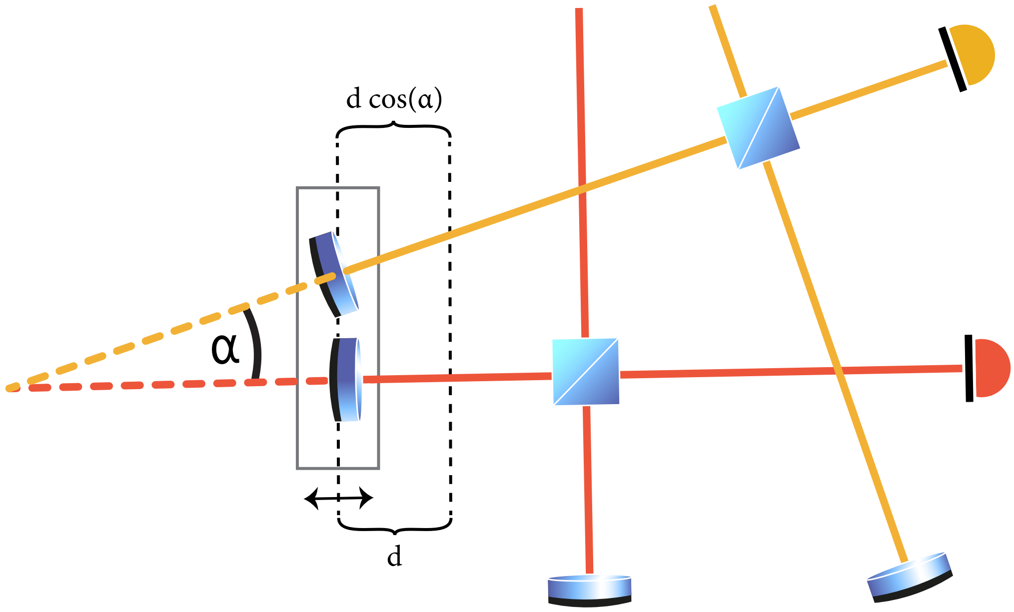

Abbildung 3.7: An illustration of the NIR and MIR interferometer performing with an angle α between them. This results in a different OPDs between the two interferometers for the same distance change of the translation stage. Such a difference in OPD results in different frequency scaling of both setups.

where α represents the angle between the two beam paths. Because the diameter of our optical components is small compared to the distance between them, α is small if both beam paths propagate through the same interferometer. However, we are in principle also able to use the second interferometer for the calibration laser beam. This can have several practical reasons. Most importantly, the transmission of the 537 nm laser is rather poor in the MIR interferometer. Therefore, a much better signal-to-noise ratio can be achieved if the VIS interferometer is used for the calibration laser. However, if this is the case, the previously introduced angle α can take arbitrary values. The OPD difference seen in the calibration laser is used to calibrate the signal. Therefore, this can create a systematic error in the scaling of the frequency axis of the signal.

Beneficial for us is that the error scales with $cos(\alpha)$. Hence, for small angles this error stays very close to zero. If the angular error remains under $3°$, the distortion to our frequency axis is negligible. This is a precision which can be easily achieved if needed. Therefore, it is possible to separating the calibration and signal beam. Nevertheless, one has to be careful when aligning the setup. Because angular deviations between the two interferometers might cause a error in the frequency calibration.

3.7 Mirror Handling

Mirrors from CMS are often built with a coating size of approximately 8mm. However, the spot size of our light source is much larger with approximately 30 mm. To minimize lost beam power, we compensate for that difference in spot sizes by focusing the light as good as possible. If necessary, we further reduce it with an aperture to the desired spot size.

We also like to be able to measure curved mirrors, especially since one of the instrument's purpose is to aid in the development of cavity enhanced spectroscopy. The cleanest way we found to measure curved sample mirrors is to use a mirror with equal curvature in the reference arm. Generally speaking the curvature can also be compensated with lenses in the corresponding arm or simply ignored. However, lenses create spatially varying dispersion because of their changing thickness which would result in a systematic error in our measurements. Simply ignoring the curvature causes the wavefronts to be curved relatively to each other. Even with large focal lengths, the relative curvature of the two wavefronts is too strong. This means that the interference pattern is indistinct and can not be captured easily. Therefore we found it the most practical under these circumstances to use curved reference mirrors.

3.8 Spectral Power Oscillation

A consistent issue was the presence of low visibility periodic oscillations in the MIR spectrum as well as in the measured phase that we referred to as ”wiggles”. The first time we encountered this effect was during the early development stages of the MIR part of the setup. At that point we used a beam splitter, which was thinner than our maximal OPD. This caused minor reflection on the back side of the beam splitter to be visible in the interferogram. We called them side bursts, since they are observable as weaker delayed copies of the center burst in the interferogram. A close description of this phenomena can be found in section 5.1.2.

As an effect of these side bursts we saw oscillations in spectrum and phase, similar to those created through double pulses. After we found out that these side bursts were caused by the beam splitter, we replaced it with a thicker one From that point on, we generally only used components which where either wedged or thicker then our maximal OPD. Interestingly, wiggles reappeared after we were able to increase the precision of our measurement. We spend quite some time searching for potential sources as we were under the impression that all optical components were either wedged or thicker than our maximal OPD. Thus, they should not be visible anymore in the interferogram. We simulated several possibilities and found that RC-tails can cause visible oscillations in Fourier space. This is shown in figure 3.8. Even though, we accidentally recorded some measurements with RC-tails, they were not found to be the source of the present wiggles.

After some time, the only components we were not able to rule out as a potential error source were the detector and the source itself. We found that both, source and detector, were covered with thin protective sapphire windows. Unfortunately, they were neither wedged nor coated in any way. To verify our initial guess we simulated the effect of a window with the corresponding properties and found them to precisely match the effect we found in our measurement. The only way to verify our guess, was to open the detector and carefully remove the window. A measurement without the protective window confirmed our guess.

The problem turned out to be more persistent in the case of the window at the light source. Because it was a Quartz-Thungston Halogen (QTH) lamp we were not able to simply remove the window because it would have destroyed the protective atmosphere of the light bulb. For that reason, we had to replace the entire QTH light source for a Globar light source. These kinds of thermal light sources contain a glowing light bar which do not need a special atmosphere. After we replaced both components, we removed all sources of problematic oscillations in our measurements.

In the current state of the setup we still find some extremely weak oscillations in the spectrum. However, they are of such an amplitude that they might have many possible sources of origin. One potential source of such weak oscillation might for example be the coating on the beam splitter. Yet, they were too weak for us to investigate further as they do not disturb our measurements anymore. Nevertheless, their origin is not yet understood and should be investigated if the need arises, as they might indicate an unknown potential error source.

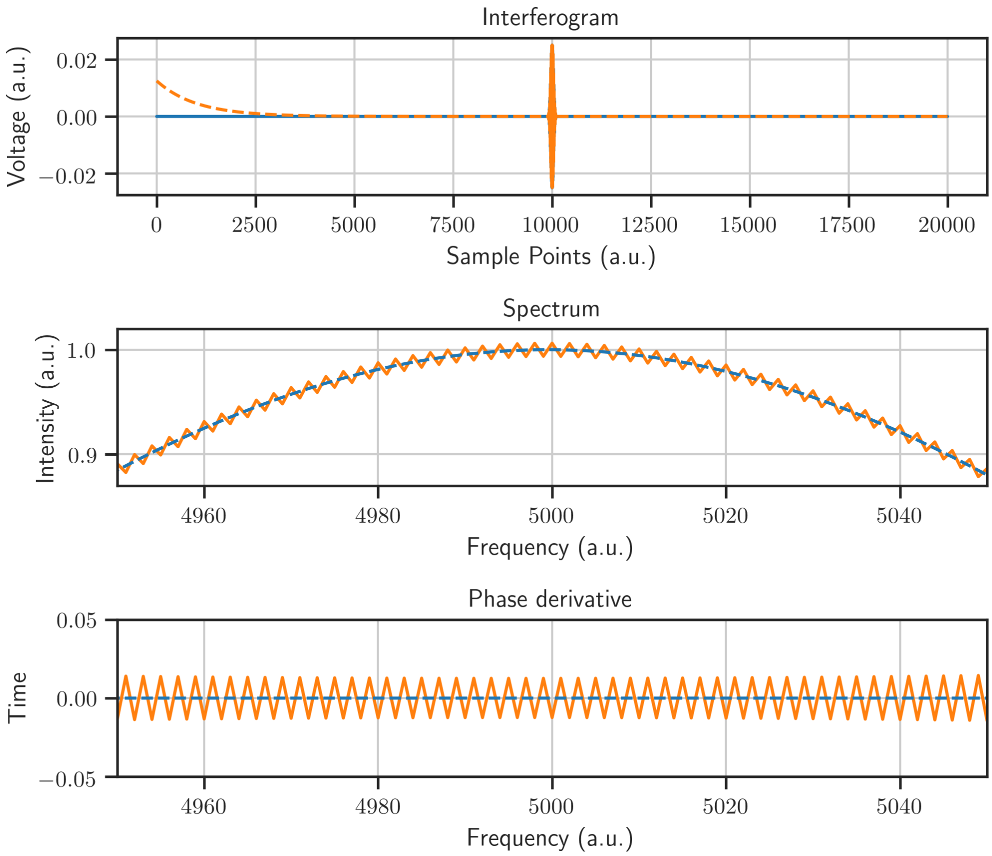

Abbildung 3.8: In the upper frame we see a synthetic Gaussian burst. The one shown in orange is identical to the other one, except for an additional RC tail at the beginning. Frame two and three show the resulting spectrum and phase of both bursts.

4 Data Acquisition and Processing

4.1 Data Aquisition

We discussed the working principle in detail in the previous chapter. We will now take a closer look at how these concepts can be applied.

Before every measurement, we have to take care of alignment. While the alignment procedure can indeed be difficult, there is conceptually nothing complicated to it. Difficulties arise because we are working in a non-visible spectral regime and our main light sources is incoherent, difficult to collimate and also low on output power. Therefore, it is only visible in a very short range of optical path differences and too weak to be visible by IR-viewer cards. It is only visible with the detector, when everything is almost perfectly aligned and the point of equal optical paths in the interferometer is found.

To find the short interference burst of the incoherent broad-band source consistently, we use the reference laser and align it parallel to the broad-band source. We align the interferometer arms in such a way that we see interference patterns of the reference laser and make sure that the point of equal optical path length between the two arms is traversed by the translation stage. With these requirements fulfilled, we should be able to see the white light interferogram on the detector.

Both, translation stage and DAQ card offer a python interface. Thus, we can control both with simple scripts. If any details are of interest, the code used is referenced in section 8.1. You can find the full source code used in the experiment in the referenced repository.

We want to use the setup to measure the dispersion of sample mirrors. However, we can not guarantee that the setup itself does not cause any dispersion to the light independent of the sample mirror. Our measurements are only sensitive to a dispersion difference between the interferometer arms. Yet, the setup might not be perfectly aligned, in the sense that both beam paths of the interferometer are perfectly balanced. If one beam path travels on a slightly longer path through a dispersive component, i.e. the beam splitter, we will measure a constant dispersion offset which we are not able to distinguish from the sample mirror. Because this would create a systematic error, we have to calibrate the setup with a reference measurement.

We use metal coated mirrors in both arms during a reference measurement because they do not create any dispersion. The dispersion measured with metal coated mirrors is guaranteed to be an exclusive contribution of fixed components in the setup. This background measurement can then be used to calibrate our other measurements by subtracting its measured dispersion (see figure. 4.1). Both, calibration and actual measurement get repeated multiple times so that we can apply statistical analysis.

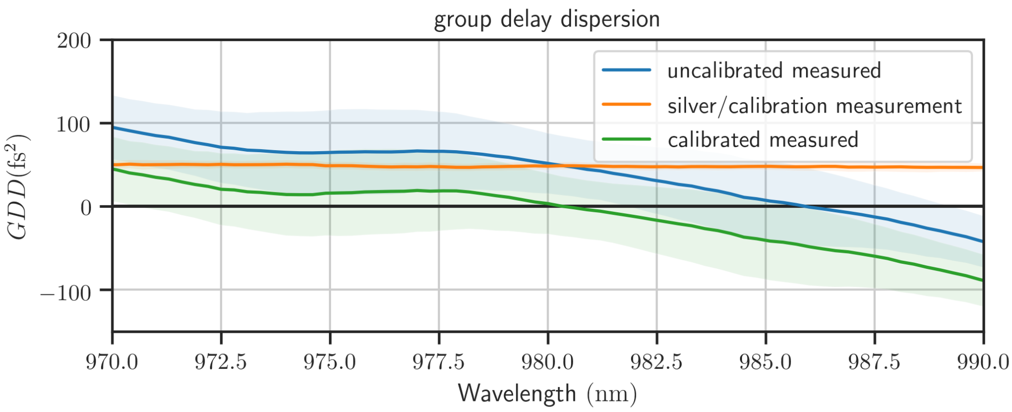

Abbildung 4.1: Exemplary measurement results are shown with a corresponding calibration measurement. Subtraction of the background GDD (orange) from the measured GDD (blue) yields the sample mirror GDD (green).

4.2 Data Evaluation

4.2.1 Operation Principle

To measure the dispersion of a mirror we capture the interference pattern of a Michelson-Interferometer for varying differences in optical path length (OPD) between the interferometer arms. It contains a reference and a sample mirror and uses a white light source. This interference pattern contains information about the phase relations between the two mirrors which can be extracted through Fourier-transformation. To have precise knowledge of the OPD we measure the interference pattern of a known laser source simultaneously. Therefore, we receive two data sets per measurement which need to be evaluated to receive the desired dispersion information.

We discussed the acquisition of these data sets in the previous section in detail. With each measurement we record two interferograms, one from the reference laser and one from the white-light source. In this section we will discuss how we can extract the dispersion information from such a measurement.

Assume we recorded a perfect measurement without any noise and perfectly equidistant OPD sample points. If this is the case, the actual data evaluation is straight forward. We would simply need to Fourier transform our white-light interferogram and calculate the phase. This would give us exact knowledge of the phase difference created between the two arms for every wavelength at which we were able to measure. To receive the GDD we need to differentiate the phase twice and end up with all the desired information.

However, several experimental problems arise during an actual measurement. One of which are variations in the OPD per sample point. If we Fourier transform a recorded interferogram,

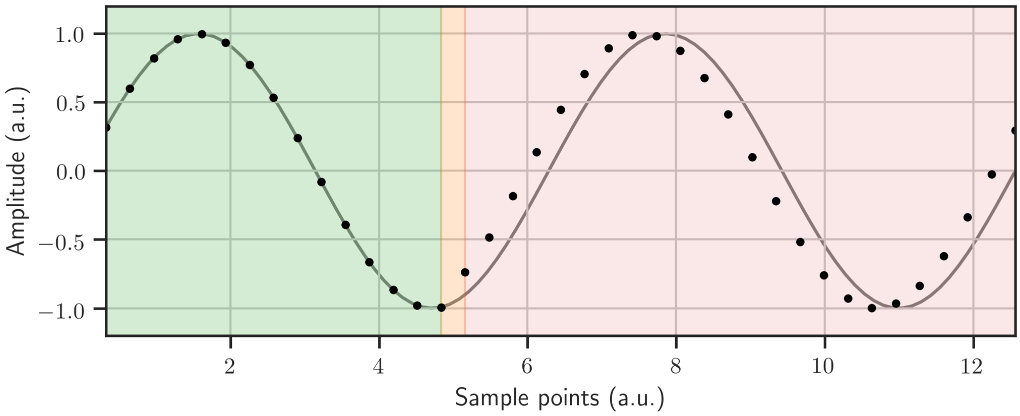

Abbildung 4.2: In gray the expected sine is shown if sample spacing is constant. The measured interferogram, shown in black, experiences a sudden phase shift between two sample points (marked in orange) caused by i.e. short term changes in stage velocity.

equal distances in OPD are expected. Otherwise the Fourier transform will not be valid and return false results. The translation stage is set to move with a constant velocity. If we sample with a constant frequency we therefore expect to have equally spaced sample points. Yet, even small changes in travel velocity impact our measurement as we need to resolved distances much smaller then the measured wavelength. Thus, we need a way to detect and compensate them.

This is done with the help of a simple diode laser that co-propagates on the same path as the white-light beam, as described before in section 3.1. As a result, a perfect sinusoidal interferogram will be detected from the laser when the translation stage is moving with constant velocity. If all sample points are equally spaced, the phase of the reference interferogram changes by a constant amount between all sample points. The exact amount of the expected phase change depends on the velocity of the translation stage, the sampling frequency and the wavelength of the reference laser. Changes in velocity of the translation stage are visible as variations from the expected phase in the laser signal. These phase changes can be used to compensate the acquired interferogram, essentially turning the reference beam into a ruler. An schematic snippet of such a signal is shown in figure 4.2.

To compensate variations in distance between sample points, one could simply check if the zero crossings of the reference interferogram are equally spaced. If that is not the case, the signal can be stretch or squeeze accordingly.

We will be using a more sophisticated method which will also take the sample points in between into account. This method was first introduced by Takeda et al. [3] and relies on phase changes in the carrier frequency f_0. We will now introduce the mechanism to extract the phase of the carrier frequency which can be found described with more detail in the original paper [3]. The interference pattern of the Michelson-Interferometer can be written in the form:

$$g(x) = a(x) + b(x)cos(2\pi f_0 x + \Phi(x)) \tag{4.1}$$

f_0 represents the carrier frequency and $a(x)$ and $b(x)$ represent unwanted irradiation variations in our signal. This equation can be rewritten into an exponential form:

$$g(x) = a(x) + c(x) \cdot exp(2\pi i f_0 x) + c^*(x) \cdot exp(-2\pi i f_0 x) \tag{4.2}$$

$$\text{with } c(x) = \frac{1}{2} b(x) \cdot exp\left\{i\phi(x)\right\} \tag{4.3}$$

ϕ in equation 4.3 is the phase of the carrier frequency which we are interested in. With knowledge of ϕ we know precisely at which OPD a sample point has been recorded. Yet, we need to separate ϕ from $a(x)$ and $b(x)$ to avoid the influence of irradiance variations in our calibration. These would disturb our calibration and introduce a new error source.

After the Fourier transformation of equation 4.2, it takes the form of:

$$G(f, z) = A(f, z) + C(f - f_0, z) + C^*(f + f_0, z) \tag{4.4}$$

where C^* is the complex conjugate of C Since the variations of $a(x)$, $b(x)$, and $\phi(x)$ are slow compared to the carrier frequency, their Fourier spectra are separated by the carrier frequency f_0, as it is shown schematically in figure 4.3.

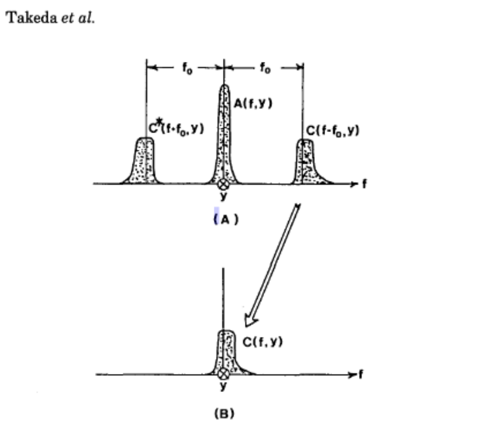

(a) (A) Schematic representation of the Fourier spectra of the interferogram. (B) single spectral band chosen and moved to the origin.

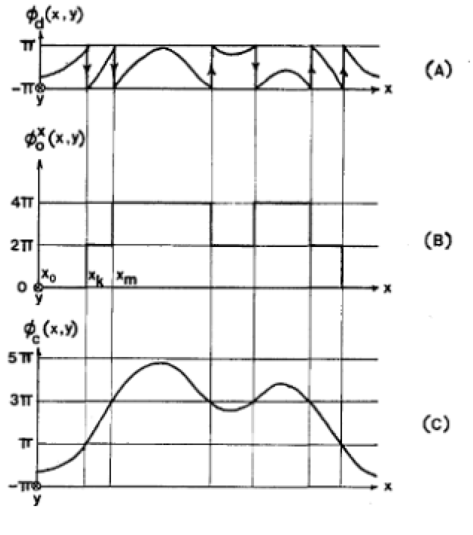

(b) Schematic representation of the phase unwrapping. (A) Example of a phase distribution having discontinuities due to the 2π periodicity. (B) Offset phase distribution to correct the discontinuities. (C) continued profile of the phase distribution.

Abbildung 4.3: Figures to visualize the unwrapped phase extraction taken from Takeda et al. [3]

C and C^* carry the same phase information because our input signal is exclusively real-valued. For this application it is therefore sufficient to only consider either one. In this case we chose to drop C^*. This is shown in the frame (a,B) of figure 4.3 where only C is still present. To obtain the phase of the carrier frequency we shift the signal so that its carrier frequency is set to zero. Under this circumstance, shifting moves elements of an array along a certain axis. Elements that are moved beyond the last position of the array are re-introduced at the first position. This is often refered to as "rolling". If we now apply an inverse Fourier transformation we will receive $c(x)$ exclusively from equation 4.2. We can now extract ϕ easily as $b(x)$ is purely real while ϕ is purely imaginary.

As for any phase, the phase extracted in such a way is undetermined by a factor of 2π. To receive an unambiguous phase we apply a process that is usually referred to as 'unwrapping'. Whenever the phase exceeds the 0 *to* 2π interval while ascending, we add a factor of 2π. On the other hand, whenever it exceeds the period while declining, we subtract a factor of 2π. This is schematically shown on the right side of figure 4.3. A more detailed description of this process can be found in [3]. This now unambiguous phase tells us precisely where the stage is located relative to its expected position. With this information we can now recalibrate the recorded interferograms and ensure that all sample points are equally spaced.

To do this, we assume only small changes in phase between every sample point because otherwise we are not able to distinguish whether a phase changed by $2\pi + \delta\phi$ or just $\delta\phi$ where $\delta\phi$ represents small changes in phase. As we will show later on, this assumption might not be valid at all times, and can cause problems in some cases.

The white-light interferometer can be recalibrated with the same method using the phase of the carrier frequency of the reference laser. The recalibrated white-light interferogram can now be Fourier transformed to receive the undistorted spectrum and phase of our signal. However, because we did not directly sample the interferogram as a function of time but rather as function of OPD, we need to calibrate the frequency axis of our Fourier transformation. As introduced before, this can also be done with the help of the reference laser. Because we know its frequency precisely we can identify the frequency bin in which the calibration laser is found with its wavelength. With the frequency scale being linear a single point besides the zero-frequency bin is enough to calibrate the full axis.

To determine the GDD, we are only left with deriving the phase with respect to its wavelength. This will be discussed in a following section. A close look at the implementation and examplery code of this routine can be found in the appendix.

4.2.2 Numerical Differentiation

The easiest approach of a numerical differentiation is a difference quotient. It can be either implemented with a forward or backwards step:

$$f' = \frac{f(x+h) - f(x)}{h} \qquad \text{or} \qquad f' = \frac{f(x) - f(x-h)}{h} \tag{4.5}$$

In both cases h represents the step size. Both, forward and backward difference share the problem that they are extremely sensitive to noise.

Imagine a sine wave with a small amount of noise added on top of it as shown in the upper frame of figure 4.4. The added errors are small enough to be hidden by the line width.

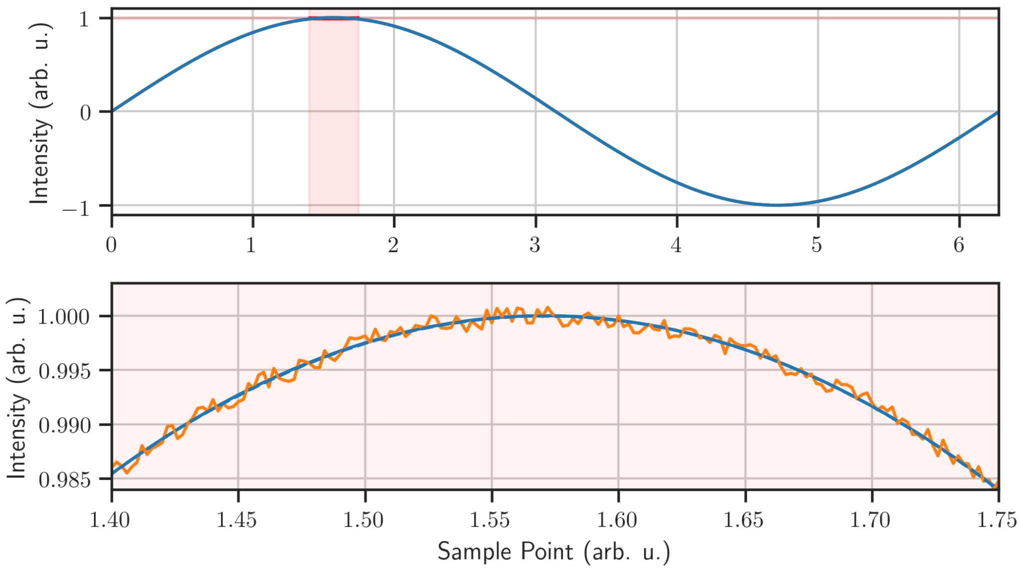

Abbildung 4.4: The upper frame shows an undisturbed sine wave. The lower frame shows a low level of Gaussian noise added to the sine. The results in the following figures are based on the sine shown in orange. Note that the noise has an average amplitude of 0.001 relative the maximal sine value.

However, in the enlarged section in the lower frame, some level of noise is clearly visible. Even though the signal to noise ratio (SNR) seems to be good, the difference quotient performs poorly when derived with a finite difference quotient of first order. i.e. a forward difference. Hence, the second derivative, which is needed for the GDD is dominated by errors and therefore not useful.

The approach which was chosen to overcome this problem is the application of filters to smooth the data before it is differentiated. The simplest approach to do this would be a running average. In that case, several data points in a certain window around a certain center point will be averaged and the original center point is replaced by the average of the window. Another way to express this is the convolution of the signal with a boxcar function. A boxcar function is zero everywhere except for a small interval where it is zero. While this approach already improves the SNR significantly it also distorts the data. This trade-off remains true for all smoothing filters. The challenge is therefore to find the filter which has the best noise suppresses for an acceptable distortion.

The filter we found best fitting for our application is the Savitzky-Golay [4] filter. The Savitzky-Golay filter fits polynomials into a window surrounding each data point and uses those polynomials to calculate derivatives. Detail on Savitzky-Golay filters can be found in section 4.2.3.

In figure 4.5, the relative deviation between the analytical derivative and the numerical derivatives are shown. An interesting effect is the high relative deviation at $\pi/2$ and $3\pi/2$. This is due the low absolute value of the derivative, hence the approximately constant absolute error is large compared to the absolute value. As a result of that, numerical methods perform worse at calculating derivatives when they are close to zero. If one compares the relative deviations of the filtered to the unfiltered deviation, one gets an idea how crucial this process is. Also take note that in the second frame the y-scale is drastically enlarged by a factor of over 100.

4.2.3 Savitzky-Golay Filter

The Savitzky-Golay filter was introduced in [4] by the eponymous authors. Its key feature is that it fits data with a polynomial of order n in a window of data points of length m centered around one data point by a least-squared method. This fit is applied to every point in the set. The center point of every fit is used as new point at that position in the fitted function. Thus, creating a fit function based on local polynomial fits. This procedure is shown in figure 4.7

We apply this routine to our interferogram to create a smoothed function. The longer the window and the lower the order of polynomial used to fit, the smoother the returned function will be. With the same logic it follows that, the smoother the resulting fitted function is, the higher the discrepancy will be to the original data. For this reason the choice of window length and polynomial is always a trade-off and a good choice of these parameters is crucial to the success of its application. Through its application, statistical fluctuation in the signal will be reduced and with it its variance. However, it will also wash out short features or even disguise them completely.

The Savitzky-Golay filter has several desirable properties as described in [5] which are worth noting. For example:

- It preserves any symmetry (even/odd) contained in the signal.
- The area under any signal curve is preserved exactly.
- The center of gravity of any signal curve is preserved exactly.
- Under the assumption of the requirements stated above and some others (shown in [5]) this filter reduces white noise optimally.

When applying a Savitzky-Golay filter a good choice of window length and order of polynomial are crucial to obtain reasonable results. In [6] properties depending on those two parameters are explored. It is shown that a feature of Gaussian shape is very well represented with a polynomial of order two and a window width equal to the size of the Full-Width-Half-Maximum (FWHM). Even though we do not apply this routine to Gaussian features exclusively, results of tests with our data sets show that the choice recommended in [6] seems

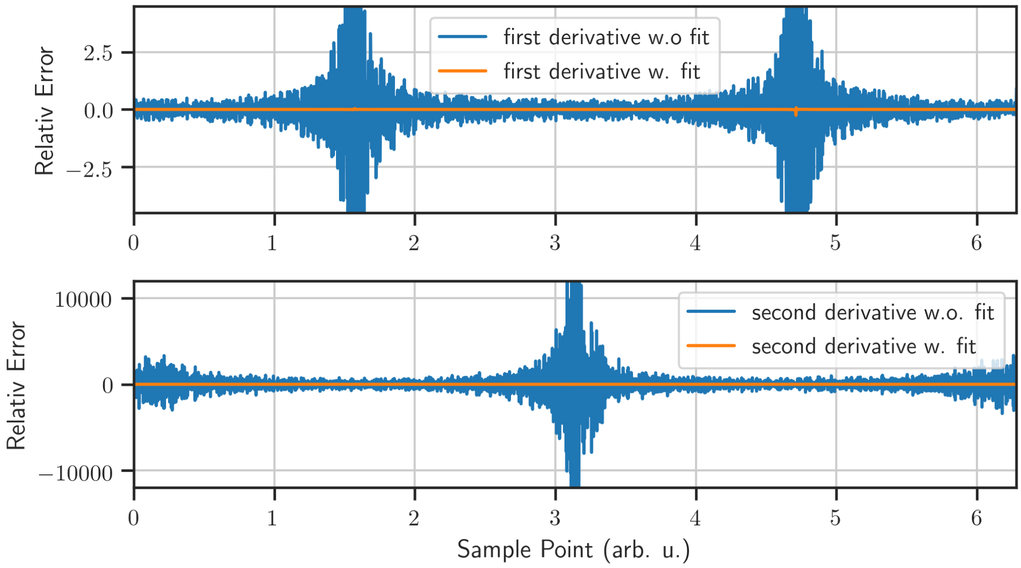

Abbildung 4.5: Relative error of filtered and unfiltered numerical derivatives. The upper frame shows the difference between the first numerical derivative off the noisy sine and and the analytical solution relative to the analytical solution. The lower frame shows the same quantities for the second numerical derivative. The blue curve shows the results without any filtering applied, while the orange curve shows the results of the derivative after a Savitzky-Golay filter was applied.

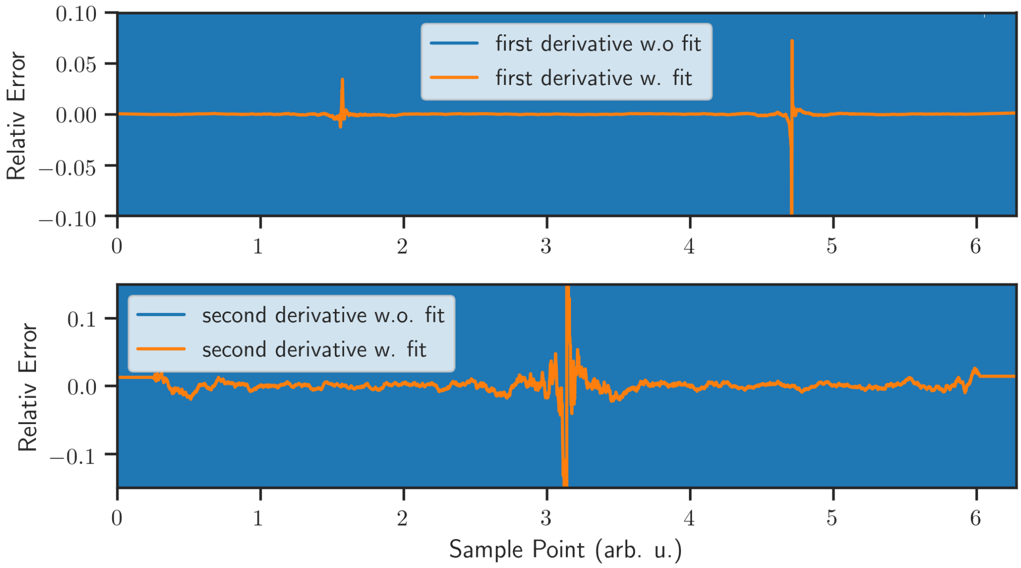

Abbildung 4.6: Shows the same results presented in 4.5 with the y-axis scaled to focus on the error of the fitted curve.

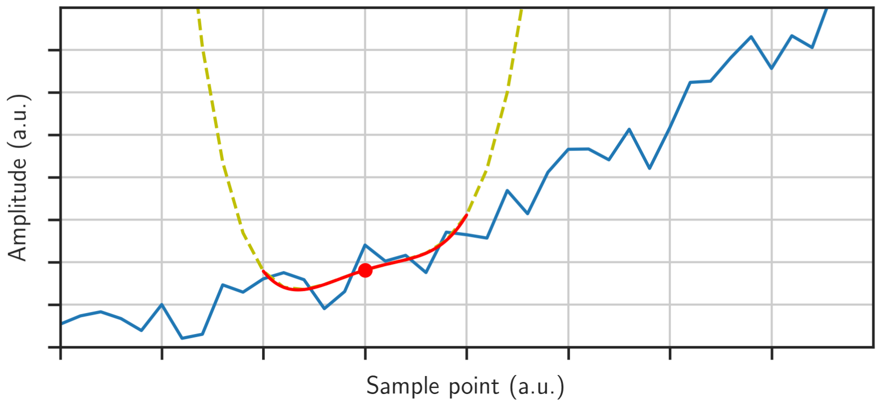

Abbildung 4.7: Exemplary working principle of the Savitzky-Golay filter. A polynomial of i.e. fourth-order is applied around a point of an arbitrary signal in a certain window. The center point of the fit is used to represent the fitted function at that point.

to be close to optimal for us as well. A detailed discussion of this choice of parameters can be found in section 5.1.6.

4.2.4 Averaging

Up until this point, only single measurements were discussed. However, to examine the reproducibility, it is necessary to be able to repeat the same measurement in such a way that the results are comparable. Additionally, we would like to be able to average data to obtain more reliable results. In principle there are several evaluation stages at which it is possible to average data.

Our first approach is to individually evaluate every single data set and save the resulting spectrum and dispersion curves. These sets can can be averaged and the according standard deviation can easily be calculated. This method is easy to implement and also stable because no remaining free parameter exist which might distort the average.

However, this leaves us with large sets of data. To put this in to perspective, during an average measurement run we usually measure 1000 data sets. In the current configuration, this results in roughly two giga byte of data. This does not only quickly clutter our memory, as we are frequently recording such measurements but also takes a large amounts of time to evaluate the data. This evaluation process takes approximately one hour on a modern machine. A convenient way to avoid this problem, is by averaging the individual interferograms during the recording procedure and only saving the averages or larger subsets. This enables us to reduce the memory and time needed to save and evaluate the data, while still having some knowledge of the measured interferograms. Because the evaluated interferograms are based on averages, this does also reduce the standard deviation of the mean. However, to be able to average the data consistently we need to properly prepare it.

Because the original data carries several degrees of freedom, such as varying start and stop position, simply averaging will distort them. Therefore we need to adjust the individual data sets in such a way that all free parameters are removed. First of all we need to calibrate the sampling distance as previously described in section 8.1. At this point we also need to compensate offsets in absolute sampling position. While the already applied calibration guarantees that all sample points are equally spaced we also need make sure that all data sets that we wish to average have the same absolute sample position. This can be achieved by interpolating all sample points to equidistant points on a common reference phase. The exact choice of this reference phase is arbitrary because its frequency in Fourier-space is determined by the frequency of the reference interferogram in the interpolated data. Through this process we can now guarantee that all sample points are not only individually consistently spaced but also relative to each other and also at the same absolute points. This is exemplary shown in figure 4.8 and 4.9.

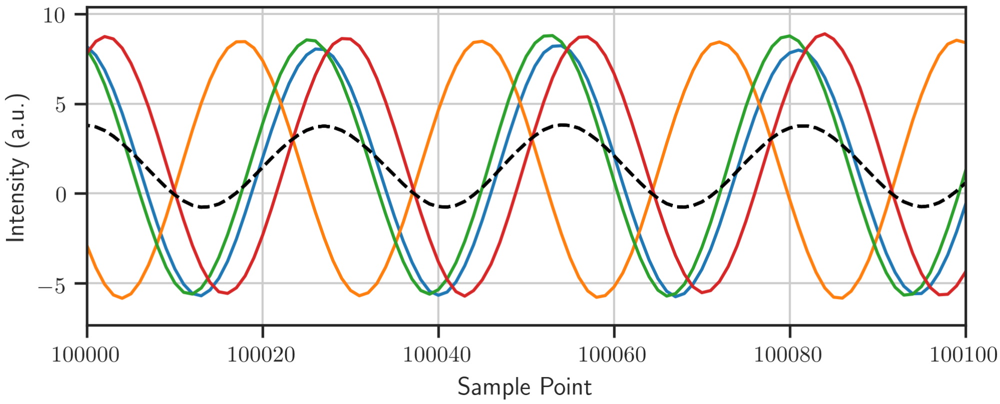

Abbildung 4.8: Reference interferograms are shown without correcting any arbitrariness in the measurement. Note, that all measurement have been equally spaced sample points individually, but not relative to each other. The resulting average of these measurements is represented by the dashed line. As one can see, this average is not representative for the individual measurements.

We can now average the original interferograms into several stacks of arbitrary size. These different stacks can then be evaluated as previously described. By calculating the standard deviation between the stacks of measurement we will receive the same deviation as if we calculate the standard deviation between the individual data sets. We will show that this statement is true in section 5.2. Through this process, we are able to reduce the memory and time needed to save and evaluate the data almost arbitrarily. A full large scale measurement run will only take up a few mega byte of space and is evaluated almost instantaneously. Nevertheless it is worth mentioning that it was rather difficult to achieve this result, since all calculations we just described have to be done 'on-the-fly' while the data is recorded. Because the time needed for individual measurements is rather short the code had to be equally fast and not too computationally demanding to disturb the actual measurement.

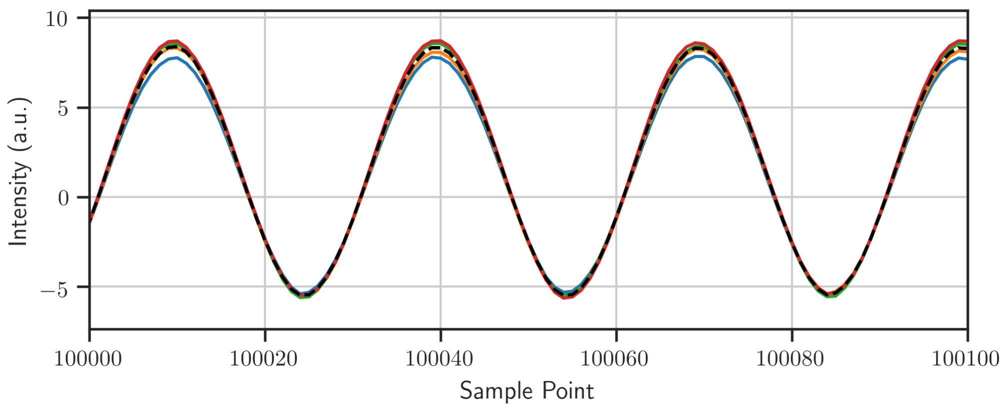

Abbildung 4.9: Reference interferograms which have been interpolated to use the same OPD values are shown. The resulting average of these measurements are represented by the dashed line. As one can see, this average is much more representative for the individual measurement compared to the average shown in 4.8

4.2.5 Data Evaluation Summary

With all the detail in the previous section one might have lost the bigger picture. Therefore we will quickly summarize the basic process of the evaluation routine in this section. A schematic diagram of this process is shown a figure 4.10.

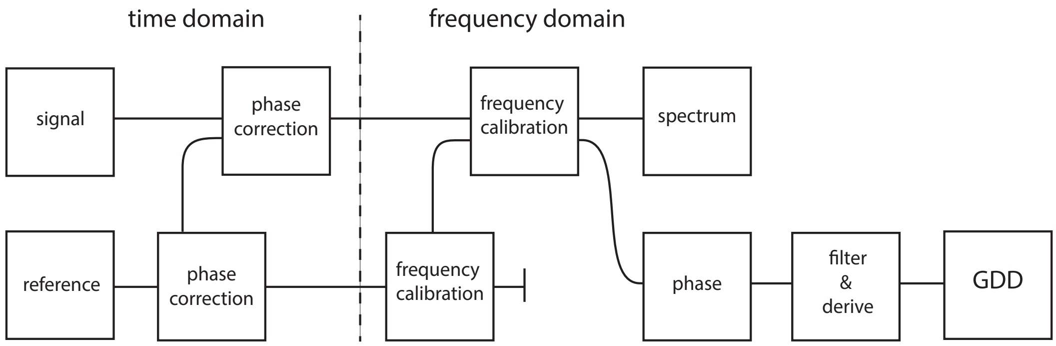

Abbildung 4.10: Flow diagram representing the structure of the evalutation routine.

We capture two interferograms. One from a light source of choice which is transmitted or reflected by the object we are measuring. This interferogram is simply referred to as 'signal' The second one is the interferogram of a spectrally narrow laser source. This interferogram is referred to as 'reference'. This second interferogram is in principle a perfect sine and can therefore be used as a ruler. If the sine is squeezed or stretched it indicates unequal sample spacing which can be adjusted by stretching or squeezing both interferograms accordingly. Additionally, we need to calibrate the frequency axis in Fourier space since we are not sampling the interferograms as a function of time. This is done with the carrier frequency of the coherent source. Because it shows itself as a sharp and distinct peak in the spectrum we can use its known frequency to calibrate the frequency axis. Due to the fact that both interferograms are sampled in the exact same way they share their frequency axis.

At this point we can directly extract the spectrum and phase of the signal. We need to derive the phase twice to receive the GDD. Because numerical derivation amplifies noise in our measurement, we need to filter our signal first to receive reasonable errors in our results. This is done with a Savitzky-Golay filter. After it has been applied, we directly receive the GDD over a broad range of wavelengths.

4.2.6 Exemplary Measurements

To this point we have discussed everything theoretically mostly without showing any experimental data. We have seen the two exemplary interferograms of the reference laser and the white-light source in figure 4.2 and 3.3. The calibration process has been sufficiently discussed before. Because the figures based on experimental data are not more informative as the previously shown schematic figures, we will only show how the carries phase of a reference interferogram is unwrapped and how it is used for calibration. This is shown in figure 4.11. The top frame shows the modulation of the phase with respect to the expected phase of the carrier frequency. If all sample points would be perfectly equally spaced we would expect a constant line. As one can clearly see, this is not the case in our measurement. These variations are mainly caused by fluctuations in the stage velocity. The stage itself monitors its position and applies correction if it differs from its set position at a given time. We found that whenever the stage experiences such deviations from its internally expected position, it tends to overshoot its correction slightly. This causing the process to repeat itself until the measured position lies in a set error margin. Therefore, causing variations in the set velocity as a result. Nevertheless, because we can extract the phase of the carrier frequency of the reference laser we can easily compensate for that. The unwrapped phase of a calibrated white-light interferogram is shown in figure 4.12.

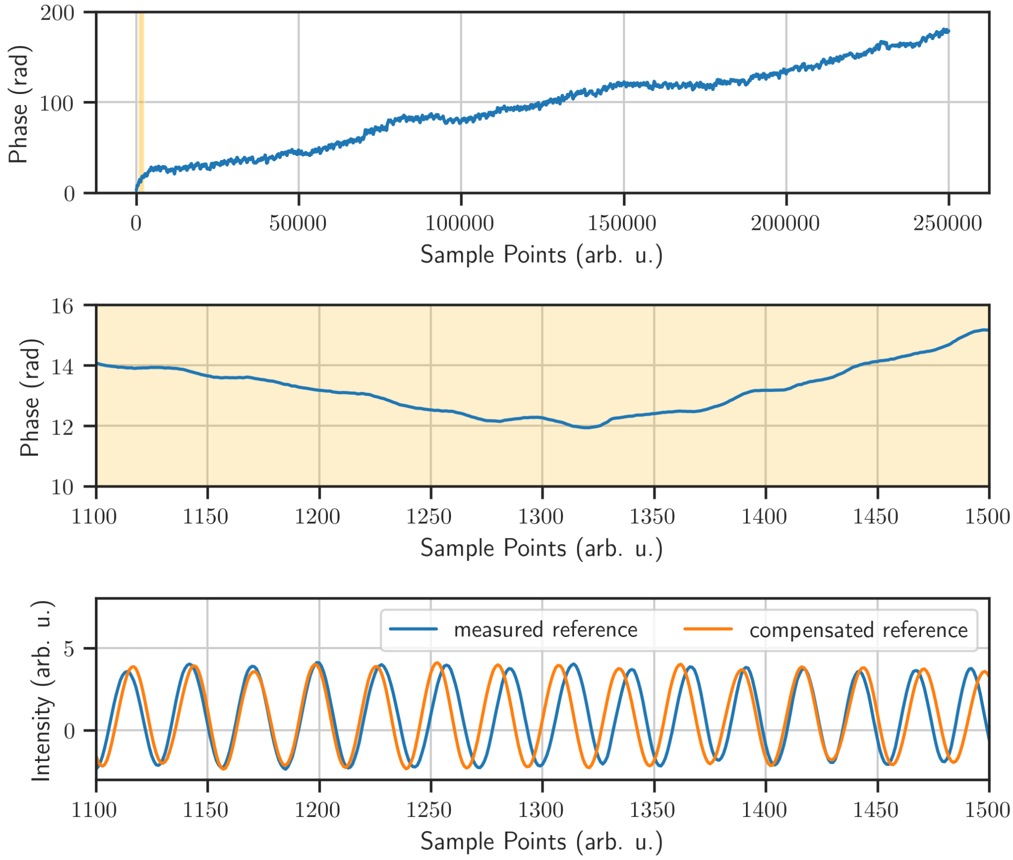

Abbildung 4.11: Exemplary phase correction with the help of the calibration laser. The upper frame shows the measured phase difference of the calibration laser compared to the expected phase. In the center frame of figure 4.11, we see a zoom on a very small region of the first frame, shown by the highlighted region. The lower frame shows an example of the influence on the interferogram due to phase differences shown in the center frame. The measured reference interferogram in shown blue, while the expected interferogram is shown in orange. The phase shift of the carrier frequency decreases in the first half of the center frame while it increases in the second half. This can also be seen in the original interferogram as it seems to be stretched in the first half and squeezed in the second.

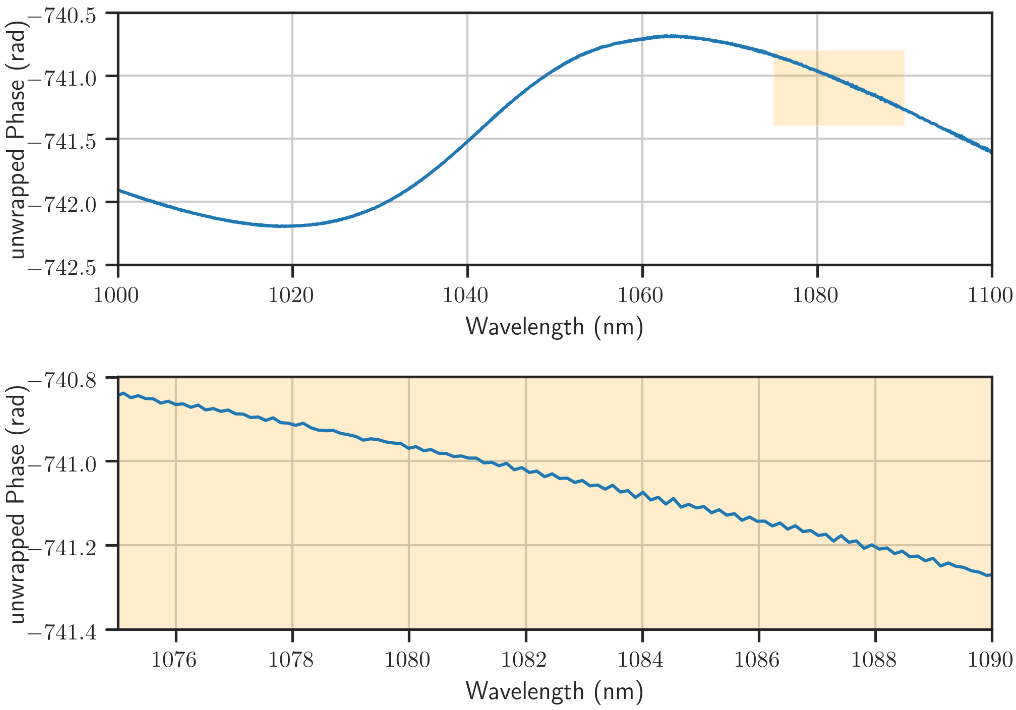

Abbildung 4.12: The top frame shows an unmodified unwrapped phase of an exemplary measurement. No filtering was applied. The lower frame shows a zoom into the highlighted region of the upper frame. While the phase seems to be perfectly smooth at first, noticeable level of noise are clearly visible in the enlarged plot.

While the level of high frequency noise in the signal seems to be almost invisible in the first frame, we can clearly see its presence in the zoom on the highlighted area in the second frame. The next figure 4.13 will show the second derivative, hence the GDD. In blue we see the second derivative base on a forward difference, while in red we see the second derivative based on a Savitzky-Golay filtered signal. Because this phase is measured in the NIR we had access to a reference measurement from the manufacturer. This reference is shown in green. While there are discrepancies between our and the measurement shown in green, they are small enough for us the assume that the general measurement principle works. To get a better understanding of all the potential error sources and their effects we will examine them one by one in the next chapter.

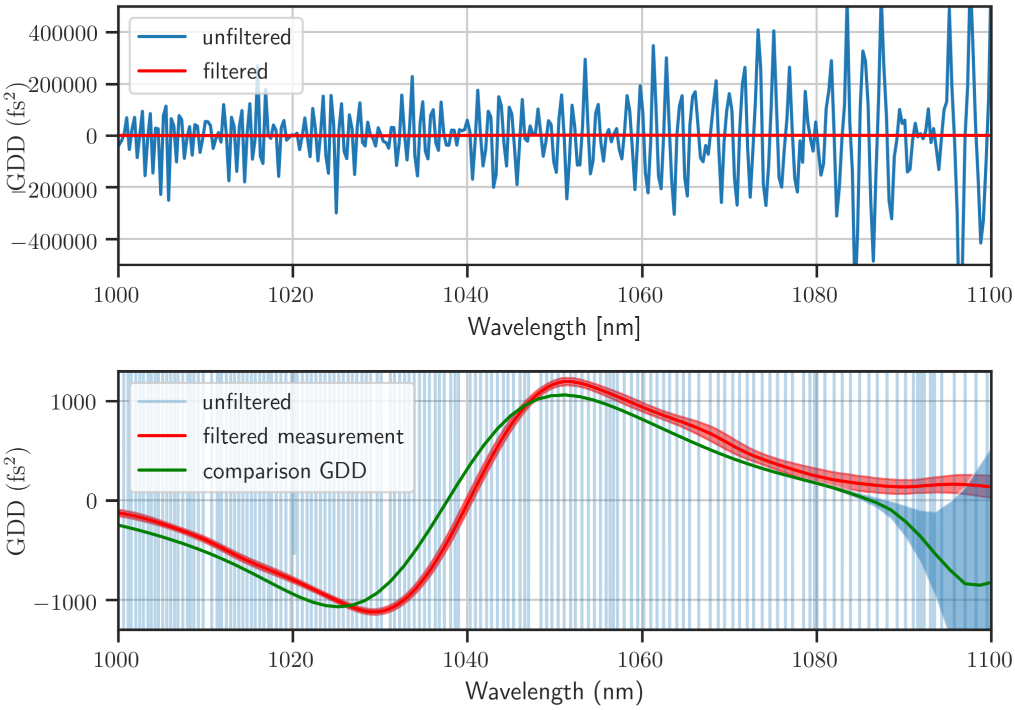

Abbildung 4.13: GDD results are shown calculated from the phase shown in 4.12. Blue shows the GDD for unfiltered phase as presented before, while red shows the results after a third order Savitzky-Golay filter was applied.

Before we will move to the next chapter we will show some more measurements and discuss them briefly. One of the available mirror sets for which we had some reference data were from Layertec. However, they were mostly only specified with expected dispersion curves based on their simulations. The only one for which a measured reference was available was the Layertec FO907022. We were given one mirror for which measured data was available from a mirror of the same coating run. This measurement is shown in 4.14. This measurement was taken during the early stages of development with the VIS prototype. Thus, the rather high amount of noise. It is to note that the measurement data given to us from Layertec contained no information on how it was measured nor did we receive any error estimate. Therefore we can only interpret it as a rough estimate Nevertheless, our measurement agrees with the data given to us in their respective error bars.

The second set of mirrors were given to us by Valentin Wittwer from the 'Laboratoire Temps-Fréquence' (LTS) research group from the University of Neuchâtel. They have a dispersion measurement setup which is able to measure the GDD in the near-IR. A comparison measurement is shown in figure 4.15. The first measurement shown (fig. 4.13) is also based on one of the mirrors given to us by Valentin Wittwer. During the development of the setup

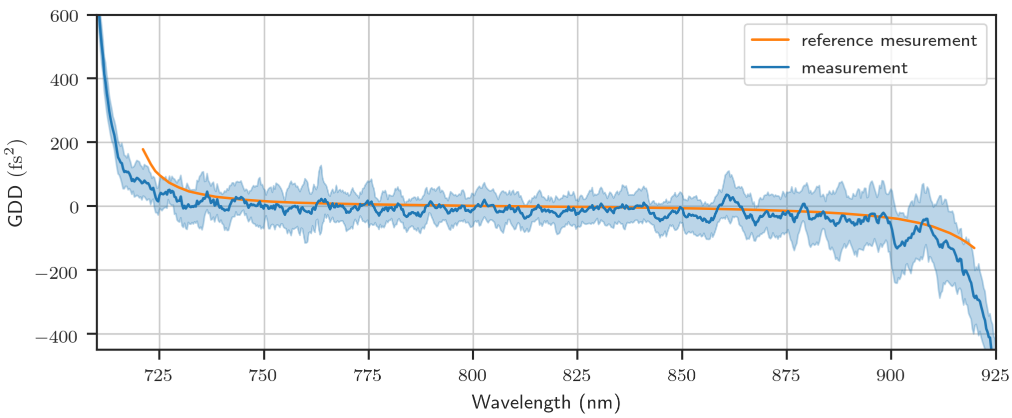

Abbildung 4.14: A measurement a Layertec F0907022 mirror is shown. The reference measurement was given to us by Layertec, however we have no information on how it was recorded or its error.

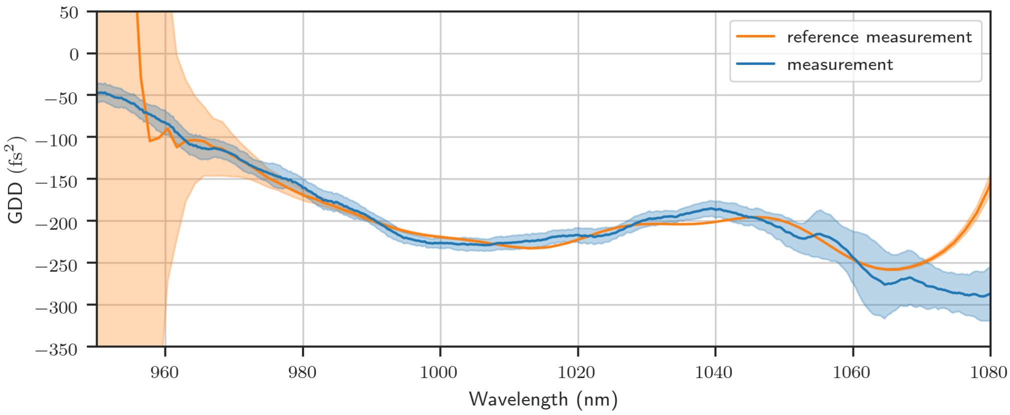

Abbildung 4.15: A measurement of the mirror 'VW0023a', with a reference taken with an NIR WLI measurment setup which uses a super continuum laser as a light source. While the error on the reference is very low in the center area, we were told by the Valentin Wittwer that significantly higher systematic errors can be expected.

we had the chance to meet him and discuss several of the potential errors and discrepancies between our measurements. These will be discussed in chapter 6.1.

5 Error Sources & Handling

In the previous chapter we discussed the working principle and behavior of the measurement setup in detail. As we are designing a tool, we need to characterize it carefully to be able to trust our measurements. Therefore, we will use this chapter to discuss potential error sources and their effect on the setups accuracy and precision. We will also take a close look at all components individually and give an estimate on its error. The benefit of this, is that it enables us to give estimates on the measurement precision which in return can compare with actual gathered data. This is helpful for identifying dominating error sources, which can then potentially be improved. Additionally, if we find a discrepancy between the expected and measured precision we can deduct that we overlook a significant error source. Finally, we hope to end up with the same total error as the statistical error that we find in our data evaluation. At this point, all errors are given as a detector voltage and will later on be translated into the resulting GDD error.

5.1 Potential Sources of Error

In this section we will examine all potential sources of error and give estimates on their on the error. We will examine the MIR part of the setup exclusively as it is our main interest. However, the major part of the results presented in the following chapter stays true for the NIR setup as well, with exception of the exact values, as they function similarly.

5.1.1 Light Source

An unstable output power of our light source results in power fluctuations of the measured interferogram and therefore creates an error in resulting GDD. The specifications of our MIR light source lists the following relative changes in output power:

- 0.1% per $°C$
- 0.01% per Hour
- Output Power Stability: $< 0.05\%$
- Color Temperature Stability: $\pm 15K$

Except for the output power stability, all of the above items can be neglected. Our measurements are too short to be affected by slow output power drifts, as they only take a few seconds. Also color temperature changes of this order are too small to be noticeable in our experiment. A color change of below 15 K after one hour results in a maximal spectral power change per spectral line of 8 %. While power changes of this size are in principle noticeable, they have to occur during the recording of a single interferogram. Our experiments showed that color changes were only noticeable after several hours. For that reason they do not effect the measurement of single interferogram sets. During a full measurement run, we collect a large set of interferograms. This process can take up to a few hours depending on the sample and the desired accuracy. Nevertheless, while the spectrum changes over the course of the full measurement the effects on the single measurements remain the same. Because the phase does not depend on the power spectrum explicitly it will not be distorted by slow power drifts.

The only noticeable effect we found are short term power fluctuation. When measured we found the power fluctuation to have a root-mean-square (rms) of approximately 2 mV in detector output voltage with an total output power of approximately 1 V. This results in a relative error of 0.2%.

5.1.2 Optical components

Dispersion offset due to unbalanced dispersive optical components

The setup is by design only sensitive to dispersion differences between the two interferometer arms. When the interferometer is not perfectly balanced it results in an constant GDD offset in our measurement which would create a systematic error. It is possible to minimize this offset to reduce the potential systematic error through precise alignment and compensating of all known unbalanced components. However, we can not guarantee that we have no dispersion offset at all. Therefore, as described in section 3.1, it is necessary to calibrate the setup and record an reference measurement with metallic coated mirrors in the interferometer. This measurement is recorded with silver mirrors in both arms of the interferometer. Silver mirrors, like all metallic mirrors can be assumed to create no dispersion. This measurement sets a baseline GDD of the setup which is then used to recalibrate our measurements. Since all optical comments are fixed during a measurement, changes over time and their resulting effect on the GDD can be neglected.

Yet, the calibration measurement itself contains a statistical error as it can only be measured with finite precision. This has to be considered in the error propagation. It is measured by the exact same routine, and so it approximately carries the same degree of error as an actual measurement. Assuming the same degree of erroer, this causes approximately an increase of our error by $\sqrt{2}$. Yet, it can not be avoided because we would introduce a systematic error of unknown size.

Stray Light & Back Reflection

The setup is required to work over a large range of frequencies. Therefore, it was not possible to use anti-reflection coated optical components. This creates back-reflections and therefore side bursts in our measurements.

The Fourier transformation of interferograms with side bursts, behaves as the Fourier transform of double pulses. The optical spectrum of a double pulse is modulated with the inverse pulse spacing. The modulation amplitude is given by the proportion of amplitude between the two pulses. Therefore, side bursts show themselves as small modulations in

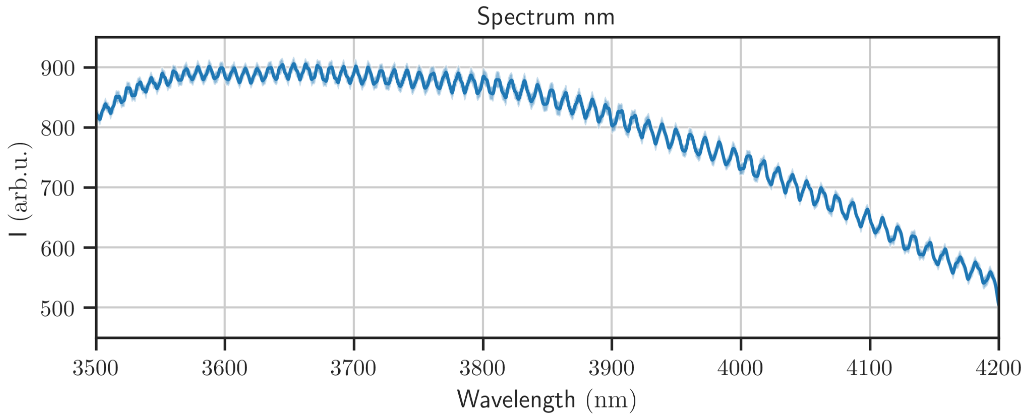

Abbildung 5.1: Output power oscillation once present in a MIR measurement.

the optical spectrum of our measurements. A characteristic example of these oscillations is shown in 5.1

The first major source of side bursts was found to be the MIR beam splitter. With a thickness of 1 mm of calcium fluoride (CaF2) we expect to find back reflection caused by the beam splitter at roughly 3 mm delay with respect to the center burst. These side bursts are clearly visible in the expected region in the interferogram shown in figure 5.2.

Even though these side bursts are considerably weaker, they nevertheless create distortions in spectrum and dispersion which that would introduce a systematic errors. Therefore, when recording or evaluating the data we have to make sure that we cut the interferogram before side bursts are present.

In principle, one could simply avoid side bursts by restricting the OPD so that they do not occur. However, as discussed in a previous chapter, large OPD are necessary to achieve a high spectral resolution. As described in equation 3.13, the resolution is anti-proportional to the maximal OPD and is currently approximately 1 nm. The other possibility to avoid this problem is to use optical components that are exclusively thicker then the maximal OPD.

After the previously described beam splitter has been replaced, we expected that all optical components, that are thin enough to cause problems with back reflections, were removed. However, we found that both our thermal light source as well as our detector are protected by 0.5 mm thick sapphire windows. To avoid the problems caused by these windows, we had to replace our Quartz-Tungsten Halogen light source with a Globar lightsource and remove the protective window in front of the detector.

We were carefully looking for additional sources of back reflection but found none. Because our measurements did not show any of the characteristic 'wiggles' caused by side bursts in the measured spectrum or dispersion (see figure 5.3), we can now exclude them as a potential source of error in our measurement.

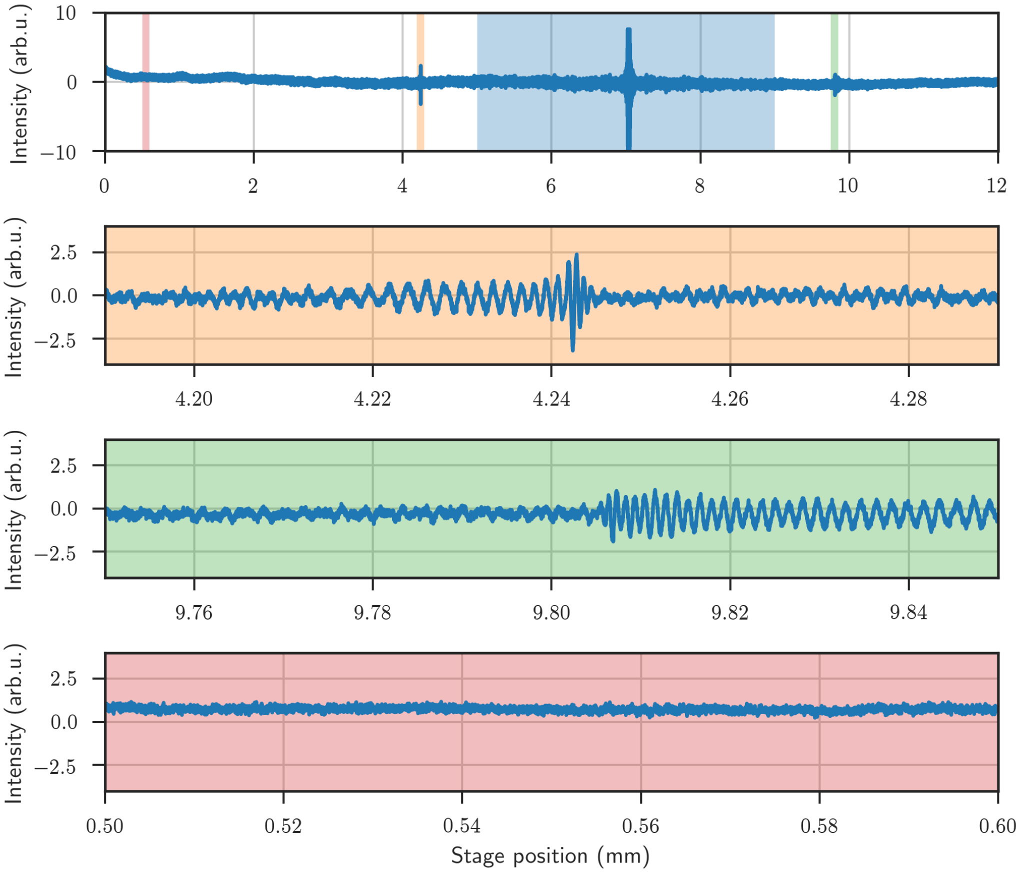

Abbildung 5.2: The upper frame shows a the interferogram at full length with the center burst at approx. 7 mm and side bursts at 4 and 10 mm. Note that this measurement was recorded while drastically over-amplifying the signal, causing the center burst to be heavily clipped. The second frame shows a zoom of the highlighted area left of the center burst, while the third frame show shows a zoom of the highlighted area the right of the center burst. The last frame shows a part of the signal which is dominated by noise as a reference.

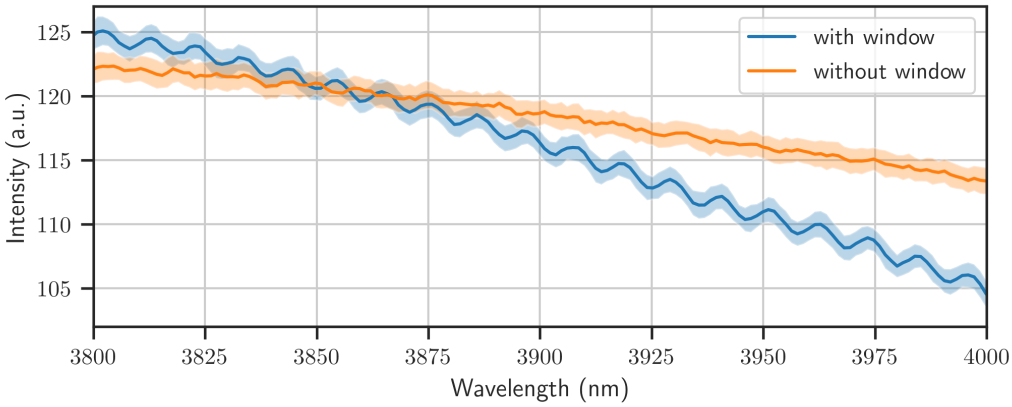

Abbildung 5.3: Output power oscillation present in MIR light source

5.1.3 Alignment Errors

Just as any other interferometer, our setup is very sensitive to alignment in the sense that minimal changes in mirror angle drastically change the interferogram pattern on the detector. However, the exact shape of the interferogram on the detector plane is irrelevant for our measurement. Only the consistency of the intensity changes along the optical axis are important. This consistency should in principle be given as long as the interferogram is clearly visible and the alignment stays the same during a measurement.

A possible alignment error is caused when the beam is not orthogonal to the mirror in the interferometer arms. When this mirrors is moved in our measurement routine we also shift the incoming and outgoing light beam and therefore change the alignment during our measurement. This introduces an unknown parameter that has an influence on the measured interferogram. Because, we can not compensated for the effects of such a changing alignment, we need to guarantee during the alignment process that both interferometer mirrors are illuminated orthogonally. Otherwise, we will introduce a systematic error.

Our experiments show that as long as all components were aligned carefully no significant systematic source of error was observed. However, slight misalignment may cause a reduced beam power or visibility which results in higher statistical errors. Since this is visible in the statistical error it does not create a problem, as such measurements can simply be repeated after the alignment has been improved.

Another important potential source of error is the angular stability of the translation stage. Due to the absence of any mechanical parts besides the voice-coil, they introduce only very low power vibrations and angular disturbances by design. Additionally, the relatively short arm lengths reduce our sensitivity to angular disturbances compared to i.e. FTIR's. This problem is not critical, as these vibrations can be assumed to be randomly distributed if no gearing is involved. Therefore, the error will be visible as a statistical error while not introducing a systematic one.

Miss-alignment during calibration measurement

A potential systematic error might be created by changes in beam path between the calibration and the actual mirror sample measurement. If the beam path changes in between the two measurements, they will not share the same baseline dispersion. Therefore, a dispersion offset will remain in the measurement of the sample mirror and create a systematic error.

This problem can be avoided through a special alignment routine. During measurement runs, only one mirror has to be switched between measuring the calibration and the sample mirror, while one mirrors stays fixed at all times. Thus, one silver mirror stays aligned at all times. Interferograms are extremely sensitive to small changes in angles between the two interfering beam paths. Therefore, a high angular accordance is a necessity for the measurement. This requirement results in negligible path differences in between measurements. Hence, additional dispersion offsets created by the misalignment of the setup can be neglected.

Extended spot size

With our extended light source we generally illuminate a spot which is roughly the size of a 1 in mirror. Through the superposition of all reflected waves, this results in averaging the dispersion during a measurement over the illuminated area of the mirror. With our design we can either focus our beam or narrow it down with an aperture. However, our thermal source is roughly 10 mm in diameter. Therefore, narrowing it down any further than that, requires us to use an aperture and by doing so losing power. This on the other hand will reduce our signal-to-noise ratio which in turn results in our measurements to be less precise. Nevertheless, the achievable spot size is small enough for most mirrors without losing a significant amount of power.

By illuminating a large portion of the mirror coating, we are usually not able to avoid defects on the mirror like a much more spatially narrow laser beam might do. However, contributions of defects are proportional to the ratio of defect area to the illuminated area on the mirror. Defects are generally small compared to their coating size and are therefore not overrepresented in a measurement. Nevertheless, this restricts us from measuring mirrors with non negligible defects easily.

Influence of Polarization

In general the components in our setup could have polarization depended properties. These might introduce a systematic error. To make sure that this is not the case, we tested the influence of different polarizations to make sure our measurement is not unknowingly influenced by them.

Three polarization angles have been tested with 45° difference. The test was performed at the VIS part of the setup because suitable polarization filters were already available. Nevertheless, we are confident to assume that this result holds true in the MIR setup as it

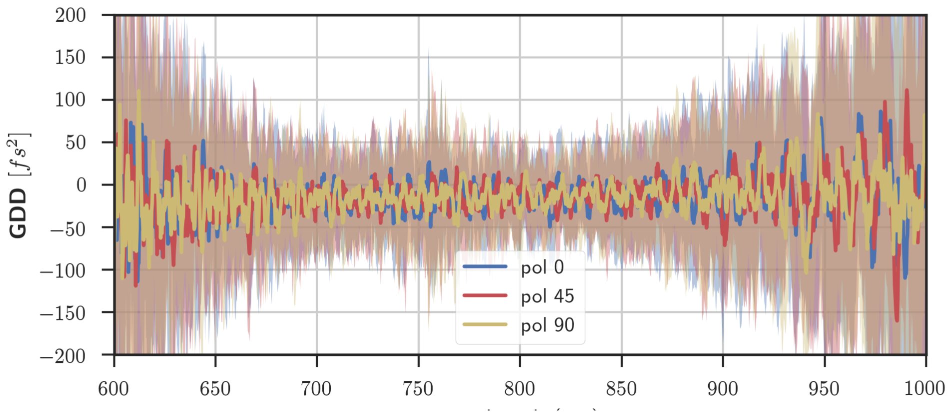

Abbildung 5.4: Results from polarization measurement. The shaded error represents the standard error marked in each respective color.

follows the same working principle. Due to a substantial power loss through the polarization filters we received rather noisy results. Despite that, it is clearly visible that the results agree in their confidence interval. Thus, we can exclude polarization effects as a source of error.

5.1.4 Detector

Noise-Equivalent-Power

A commonly used measure for detector noise is the 'Noise-Equivalent Power' (NEP). Its refers to lowest ingoing power that creates a signal equally strong as the detectors noise over a 1 Hz bandwidth in its sensitive spectral range. This value is achieved at the wavelength λ with the highest response R_{max}. The relation to generalize the NEP values for the full spectral range is defined by:

$$NEP(\lambda) = NEP_{min} \cdot \frac{R_{max}}{R(\lambda)} \tag{5.1}$$

Where $R(\lambda)$ represents the detector response for given wavelength λ. The input power detected, which is equal to the noise power at a given wavelength λ and bandwidth BW is then given by:

$$P_{min} = NEP(\lambda) \cdot \sqrt{BW} \tag{5.2}$$

With this information and the assumption of white noise, one can calculate the expected noise rms for a detector in a given bandwidth. However, we will be using our detector with its full bandwidth and in its full spectral range at all times. Therefore, we can simply characterize the detector with a fixed noise rms.

The detector noise can easily be measured since it is independent from its incoming spectral power. The average rms of our MIR detector (PDA20H Thorlabs) was found to

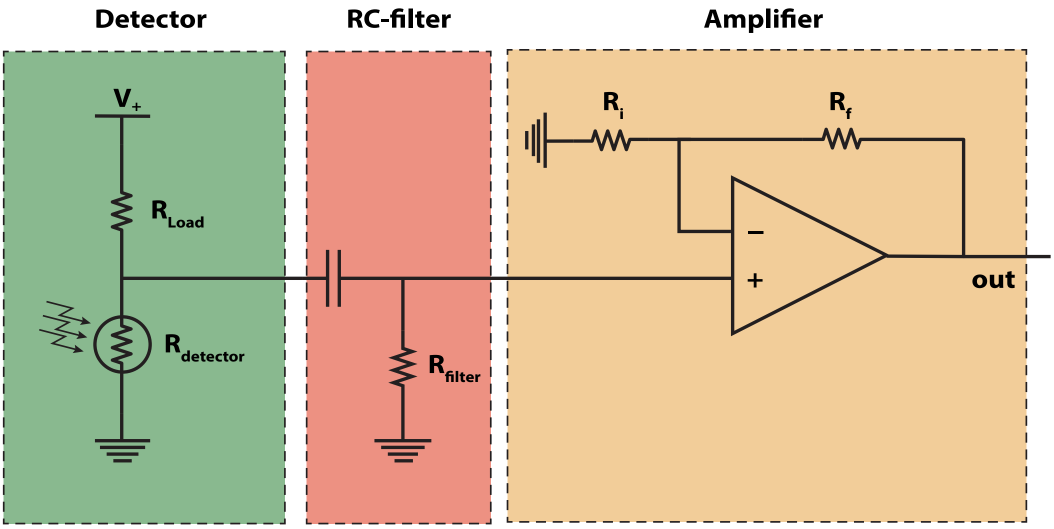

Abbildung 5.5: A schematic circuit drawing of an AC coupled amplified PbS or PbSe detector.

be approximately 2.5 mV. Keep in mind, that the detector output will be amplified before it is captured and with it its noise. Hence, the detector noise, as all noise sources before the amplifier will have an much higher impact then those who are not amplified. With an approximate amplification of the signal by a factor of ten, all unamplified error sources need to be ten times higher to cause the same amount of error as the preceding ones.

Detector linearity

A more difficult topic is detector linearity. For an ideal detector a perfectly linear response between input power and output voltage is expected. While in practice these relation can have an arbitrary shape. Exemplary detector responses are shown in figure 5.6. Due to the fact that all MIR detectors that we used were AC-coupled, we were not able to simply record a detector response while tuning through the optical input power.

Our main IR detector was amplified and based on lead selenide (PbSe) (PDA20H Thorlabs). We will discuss this type of detector specifically, while most concepts hold for all AC-coupled detectors. In the case of a PbSe detector, the actual photo detector does not produce a current when illuminated like most other photo detectors do, but instead reduces its electrical resistance. Because we would still like to measure voltages, we need to transform the photo detector resistance into an output voltage. This is commonly done with a circuit as shown in figure 5.5: To avoid the $\frac{1}{f}$ noise response of the photo conductor, where f represents the frequency of the noise, the basic circuit will be AC coupled with an RC circuit. In the case of our detector this signal was also amplified to achieve a convenient output range of $\pm 10\ V$ for common short term power differences. As a result of this configuration,

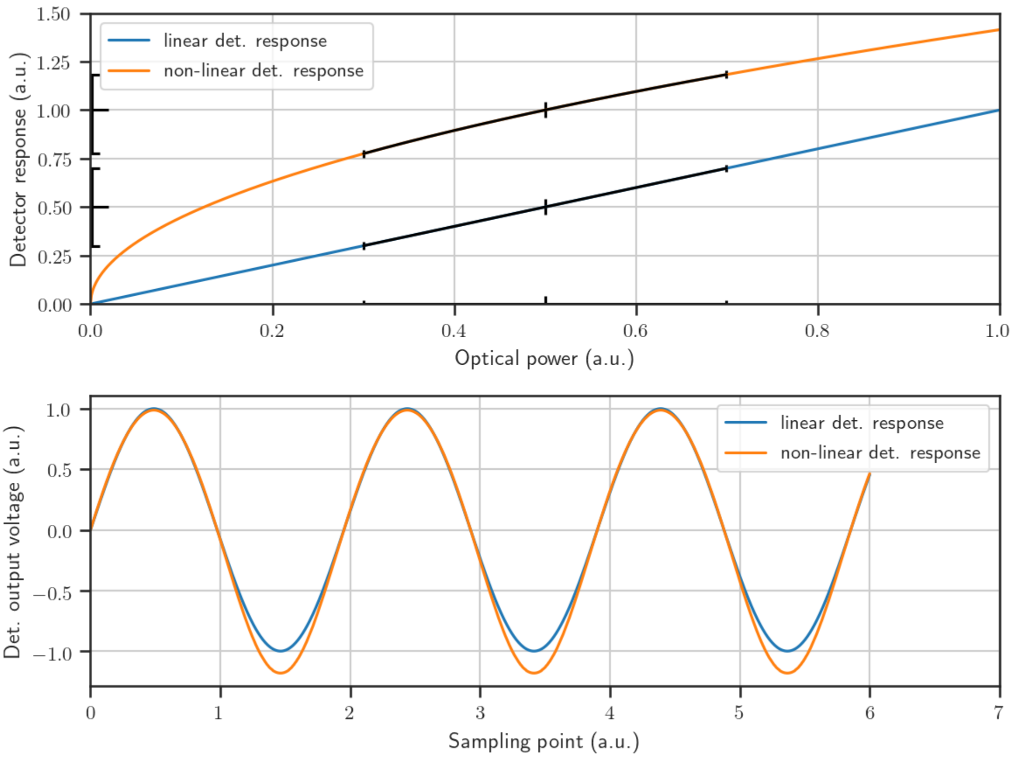

Abbildung 5.6: In the upper frame we see examplary detector responses. The blue shows a perfectly linear response while the orange response shows strong non-linearities. The resulting effects on a measured sine signal for these exemplary responses is shown in the lower frame.

it is not easy to measure the linearity of the detector, due to the fact that the AC coupling obscures the DC position on the detector response curve.

When measuring an AC signal, the absolute optical power at the detector remains unknown. Hence, the x-position on the graph shown in figure 5.6 is also unknown. The output range of the detector is only a small portion of its input range, as it is highly amplified. As different measurements do not necessarily have the same power at the detector, one can not calibrate all measurements with the same calibration measurement. Thus, it would be necessary to record a calibration measurement for every average optical input power to be able to perfectly compensate non-linearities in the response. However, it is then also needed to measure the average detector power during a measurement to apply the proper compensation. This has not been done during our measurements and might be a potential uncharacterized source of error which will be discussed in section 6.1.

5.1.5 Amplifier

Measuring noise of amplifiers is a sophisticated subject by itself. To characterize the amplifier we use a model presented in [7]. It assumes a well known external noise source N_S and an internal amplifier noises source N_{Amp}. Both of which will be amplified by a gain factor G. This results in a total output noise N_{out} of

$$N_{\text{out}} = G(N_S + N_{\text{Amp}}) \tag{5.3}$$

As our amplifier is variable in gain we need to measure its gain for all noise measurement as well. This can be done by using a stabilized voltage source as a reference. With it, the gain factor G can easily be measured by measuring the average output voltage while comparing it to the voltage source output. With this routine we are able to measure the amplifiers internal noise precisely because N_S and G are known with high accuracy.

Our measurements show N_{Amp} to be 2.5 mV. Hence, with average gain factor of 10 the amplifier noise and all preceding random noise sources get also amplified by a factor of ten.

Amplifier linearity was also examined. In our measurement range of ±10 V and precision which was limited to 5 mV by the DAQ card, we did not find any significant non-linearities.

5.1.6 Data-Aquisition-Card

Variation in sample point timing

When applying a discrete Fourier transform, one generally assumes that all data points are equally spaced. Even though routines which use unequally spaced sample points exits, they are computational more expensive and it is necessary to know the distance between all sample points. The sampling timing of the DAQ unit may underlay statistical fluctuations which will violate the assumption of equally spaced sample points.

Let $f(\Delta t + \delta t)$ be a function with Δt being the distance between sample points and δt being a small variance. Because δt is always smaller then Δt the error created by δt can never by larger then then $|f(\Delta t) - f(\Delta t + \delta t)|$. In the current configuration of the setup we purposely over-sample which drastically decreases the potential error from changes in sample point.

The specification sheet also shows an extremely low variance in sample timing of 50ppm. Therefore we can safely neglect variation in sample point timing as a significant source of error. To verify this claim, we simulated variations in sampling timing. The simulation results are shown in figure 5.7. We drastically overestimated the variation in sample timing to have a standard deviation of 10% of the sample distance, assuming a Gaussian distribution. The implementation detail of the simulation are discussed in section 5.2 As one can see, the errors created by a varying sampling timing are very low and, as we will find out later, negligible compared to other noise sources even when overestimated by a factor of 2.000.

Discretisation error

Another potential source of error created by the DAQ is a discretization error. It digitalizes the analog input into a finite amount of levels in the input range. The currently used DAQ

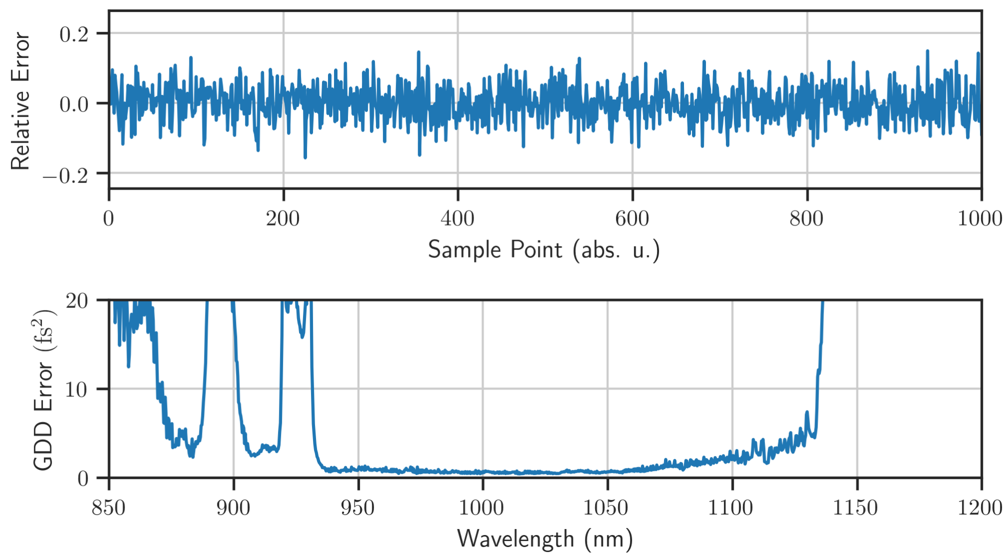

Abbildung 5.7: The upper frame shows the relative error on the sampling timing which was added to our data set. The lower frame shows the resulting error on the GDD caused by that. With an error of below 1 fs^2 in the spectral region of interest, this effect is vastly overshadowed by other error sources.

has a resolution of 12 bit spread over an input range of ±10 V. This results in a discretization level separated by approximately 5 mV. Hence, changes in detector voltage smaller then 5 mV might be mapped to the same voltage by the DAQ and therefore be unnoticeable. This of course, distorts the signal and causes an error in the calculation of the dispersion. When we assume that changes in detector voltage between sample points are generally larger then the distance between discretization levels we can conclude that the created error can be represented by a uniformly randomly distributed noise between 0 and -5 mV.

The propagation of this error has been simulated for a DAQ with 12, 14 and 16 bit. The results are shown in figure 5.8. As one can clearly see, errors caused by the discretization are clearly contributing with approximately 5 fs^2 to the total error in the case of a 12 bit DAQ as long as the total signal amplitude uses the majority of the input range. Nevertheless, this error scales proportional to $\frac{V_{max}}{V_{used}}$. With V_{max} being the maximal input range and V_{used} the maximal used voltage range.

Differentiation of noisy signals

Numerical differentiation is an unstable operation which acts as an error amplifier on the acquired data. However, it is inevitable for our task. The error amplification of an ideal discrete differentiator is proportional to the frequency of the differentiated signal. Hence, it

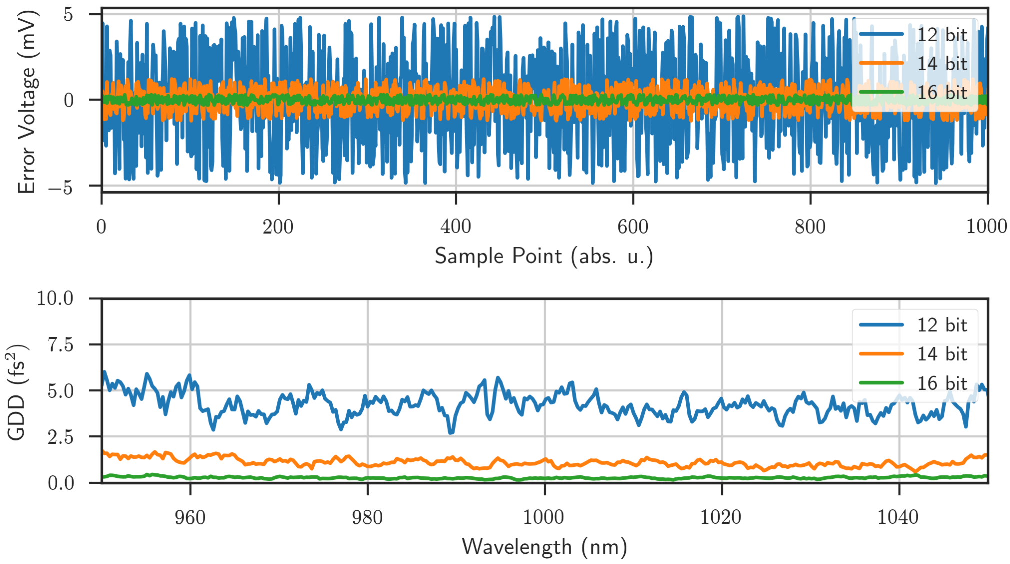

Abbildung 5.8: The upper frame shows an exemplary error added to the signal by the discretization in the DAQ card. Note that this error is uniformly distributed. The lower frame shows the created standard deviation by the discretisation. Note that we are currently using a 12 bit DAQ card.

is beneficial to apply some sort of low-pass filter.

The Savitzky-Golay filter which we apply satisfies this requirement. Its working principle is described in section 4.2.3. The error amplification reduction of a Savitzky-Golay filter is proportional to the window length and also performs better the lower the order of fitted the polynomials is. A detailed analysis of this behavior can be found in [6]. Since we do not have an upper bound for frequency components in the measured phase we can not find an 'optimal' application when applying a Savitzky-Golay filter. Because using longer windows and lower polynomials deforms the signal, we rather have to find a reasonable trade-off between noise suppression and acceptable distortion.

Using a window length of the size of the minimal resolution does not provide any noise suppression. As discussed in section 4.2.3, we need to extend the window over several points to achieve an improvement. To resolve features of Gaussian shape, a window length of the size of its full-width-half-maximum (FWHM) is sufficient when a polynomial of second order is used. Because our resolution changes over its spectral range, the width of resolvable features for a fixed windows size will change as well. However, the advantage of a fixed window size is that the error supersession does not scale with the fitted wavelength but stays independent of it. In the process of finding appropriate parameters we simulated the effect of different sizes of window sizes and degrees of polynomials. The results can be shown in figure 5.9 and 5.10.

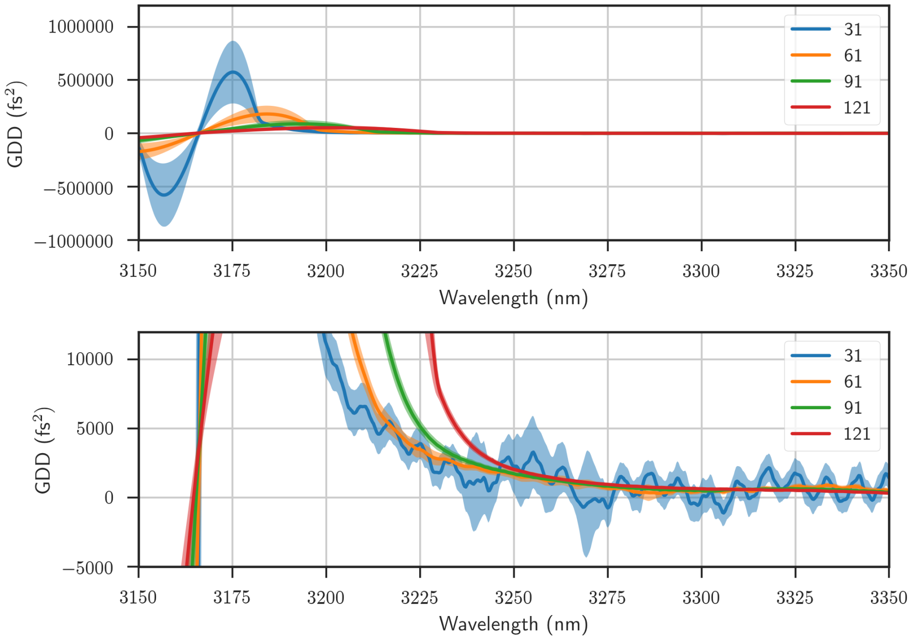

Abbildung 5.9: The distortion effects of a low order Savitzky-Golay is shown for different window lengths. Noise suppression increases with larger windows. However, so does the distortion, as short features will be broadened. An ideal trade of can only be found with precise knowledge of the frequency components in the modeled curve.

Through the choice of window width of 61 points and a third order polynomial we are able to perfectly represent a Gaussian feature of 5 nm FHWM at an average wavelength of 2.5 μm. At the same time, we will still be able to preserve Gaussian lines with half the width, of 2.5 nm with a 0.8 height response. This was sufficient for all applications we encountered so far. If one suspects important shorter features, one can simply reduce the window width to be able to represent them. However, this will introduce higher statistical errors.

5.1.7 External Error Sources

Vibrations

As with every interferometer, our setup is very sensitive to vibrations. This is a result of the high susceptibility to changes in optical path length that are created by vibrations in our setup. The only potential source of vibration our the setup is the voice coil translation stage whose main feature is to have extremely low power vibrations for a translation stage. To isolate the setup from external vibrations, we used sorbothane feet to isolate the breadboard from the already damped optical table. The sorbothane mostly suppresses the noise created

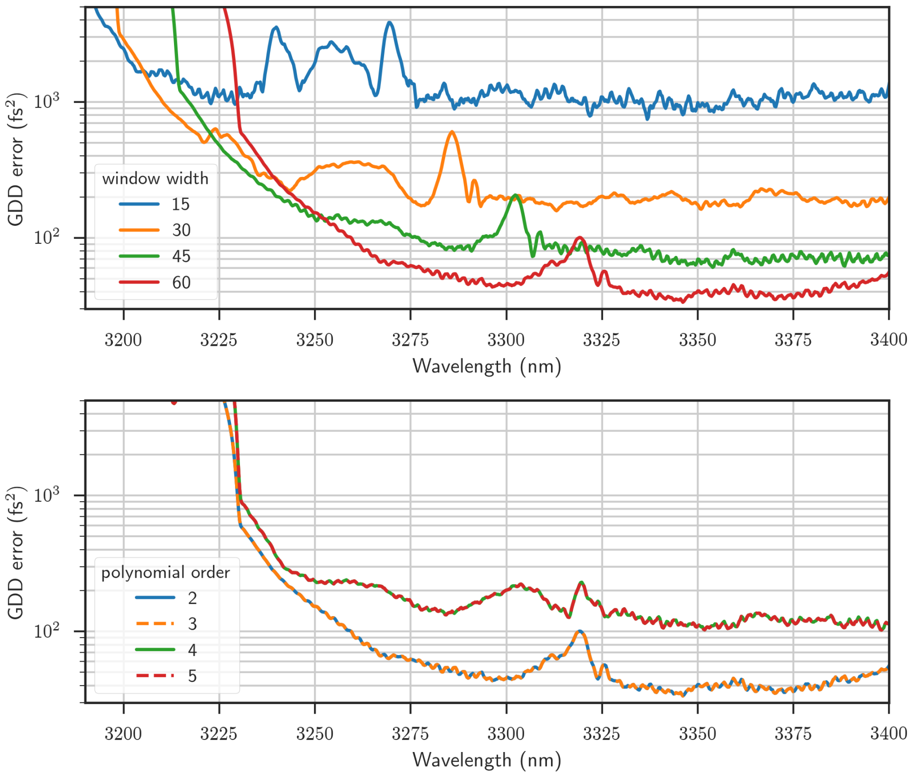

Abbildung 5.10: In the top frame we see the standard deviation of the GDD for several window widths for a third order polynomial. The stop band of the measured mirror started at approximately 3225 nm which causes the GDD to have en extremly sharp feature at this wavelength. Note, that this feature dissipates into to region above 3225 nm for wider filter-windows. In the lower frame, the standard deviation of the GDD is shown for the same mirror for several different polynomial orders with a fixed window with of 60 points.

from other people working on the same table. To reduce noise created by temperature drifts, air drifts and acoustical noise, a styrodur box was build around the breadboard standing on the optical table. While the presence of strong vibrations was clearly visible before we installed sorbothane feet and the styrodur box, we were not able to inflict any visible oscillations in our measurement when actively trying to disturb it. Experiments testing the vibration isolation show that measurements in a quiet environment show no visible differences in the dispersion and its standard deviation, compared to a very noisy lab with people working on the same table. During a measurement we capture at least a hundred interferograms over at minimum several minutes. While isolated disturbances through vibrations caused by people working in the lab are of course possible they are expected to only affect a small portion of the recorded data. Therefore we do not expect them to have a considerable impact on our measurements due to the high amount of measurements used for averaging. Additionally, we will be able to see such disturbances in the statistical error and, if in doubt, are therefore able to identify and repeat them if necessary.

Temperature Drift

Several components of this setup are temperature sensitive. In principle, this could create significant disturbances in the measured GDD. However, as described in section 5.1, all dependencies of components that are temperature dependent are weak compared to other sources of error. Furthermore, we do not expect any sudden temperature changes because, not only is the whole lab temperature stabilized but also the setup itself is isolated by a styrodur box to make sure sudden changes in lab temperature do not affect the setup quickly. With this we are safe to assume that errors caused by short term temperature drift are negligible.

5.2 Simulation of Error Propagation

To find limiting error sources, we are interested in what kind of errors in measured data create what type of errors in our results. Because our setup is rather complex, we can not find a simple analytical solution for the error propagation. This is mostly due to the complexity that is introduced to the derivation of the phase and its preceding filtering. These processes introduce a complex dependency on the noise frequency. Therefore we instead simulate the propagation of error in measurement data through the evaluation routine.

Regardless of what kind of behavior we would like to simulate, we are always able to do so by manipulating the captured voltage values. For example, if we would like to know how our results would change if we vary the sampling timing, we can simply interpolate our data and therefore are able to represent them as voltage changes. This process might be more complicated for more complex changes, nevertheless, it is always possible.

To be sure, that the changes in our results originate from the added changes, we will start by making several sanity checks. We use a single measurement set containing the reference and signal data trace to create a set of exact duplicates of them. If our evaluation routine is consistent we expect that each data set returns the exact same result and will thus, have a

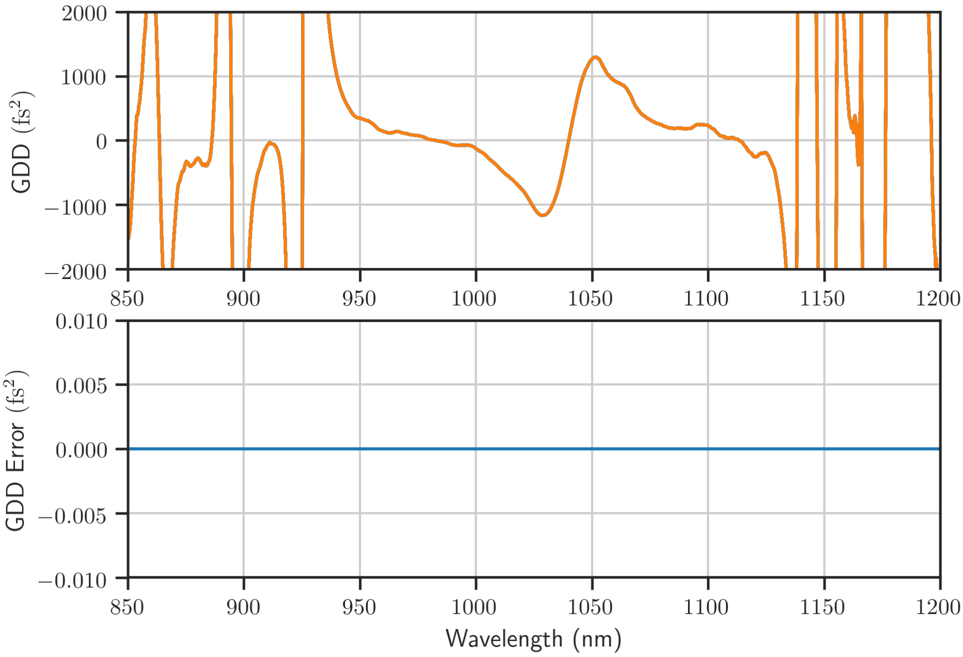

Abbildung 5.11: Shows the GDD of a set of identical interferograms to test if any unexpected behaviour can be observed. We expect it to be perfectly zero for all points. Any variations might indicate errors or misconception in the data evaluation.

vanishing variance. This can easily be verified and is shown to work as expect in figure 5.11.

After this short test, we continued with the following sanity checks. We expect the error on phase and spectrum of the Fourier transformed signal to scale linearly with added Gaussian noise on our test data set. Additionally, the resulting error should not depend on the absolute noise amplitude added but rather on the ratio between signal and noise amplitude. To simulate this, we added random Gaussian noise to the data sets. The added noise was random for each set independently. Hence, the noise was different for every data set. This process was carried out for three different signal-to-noise ratios (SNR). The full process was repeated with three different signal amplitudes, to test if absolute signal or noise amplitudes have an effect. The results of this are shown in figure 5.12. As one can see, these assumption hold very well, especially for lower SNR's in which we are particularly interested.

Through this process we were able to simulate all known sources off error and compare their contribution. In the following section we will discuss their individual impact and compare the measured to the simulated data.

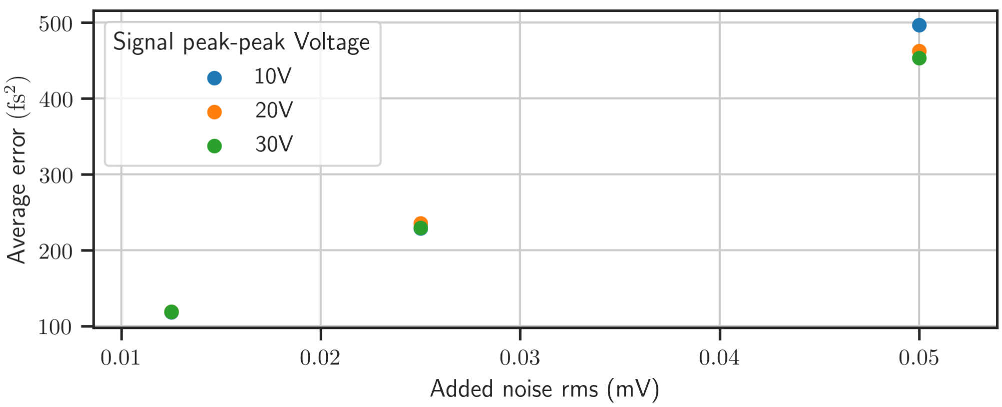

Abbildung 5.12: Shows the average GDD error of a narrow spectral range for several different signal and signal-to-noise conditions. This is to test whether the error scales linearly to the signal-to-noise ratio.

5.3 Achieved Measurement Quality

To summarize, we were able to identify the following major noise sources:

- Light Source: 2 mV (Amplified by Gain)
- Amplifier 2.5 mV (Amplified by Gain)
- Amplifier 2.5 mV (Amplified by Gain)
- DAQ 3.7 mV

To find an estimate for the resulting GDD we use the simulation routine described in 5.2. However, this estimate depends on several factors that a varying from measurement to measurement. For example, the measurement precision depends strongly on the captured signal intensity which depends on the reflectivity of the mirrors measured. This affects the necessary amplification to compensate for discretization errors and so on.

To validate our estimate we tested it on several different measurements. The produced results were consistent with each other. We will present one simulation exclusively, based the representative measurement shown in figure 5.13.

As one can see, in the stop band of the tested mirror we have an average GDD error of approximately 50 fs^2. In the lower frame of the figure, we also see the simulated error estimate with experimental error estimation from the original data set. Because the amount of error predicted by our simulation matches the error found in our measurement very well, it looks like we have found all major error sources and will discuss ways on how to improve them in section 6.1.

Now that we understand the effect of individual error sources, we would like to know how the error scales when several measurements are averaged.

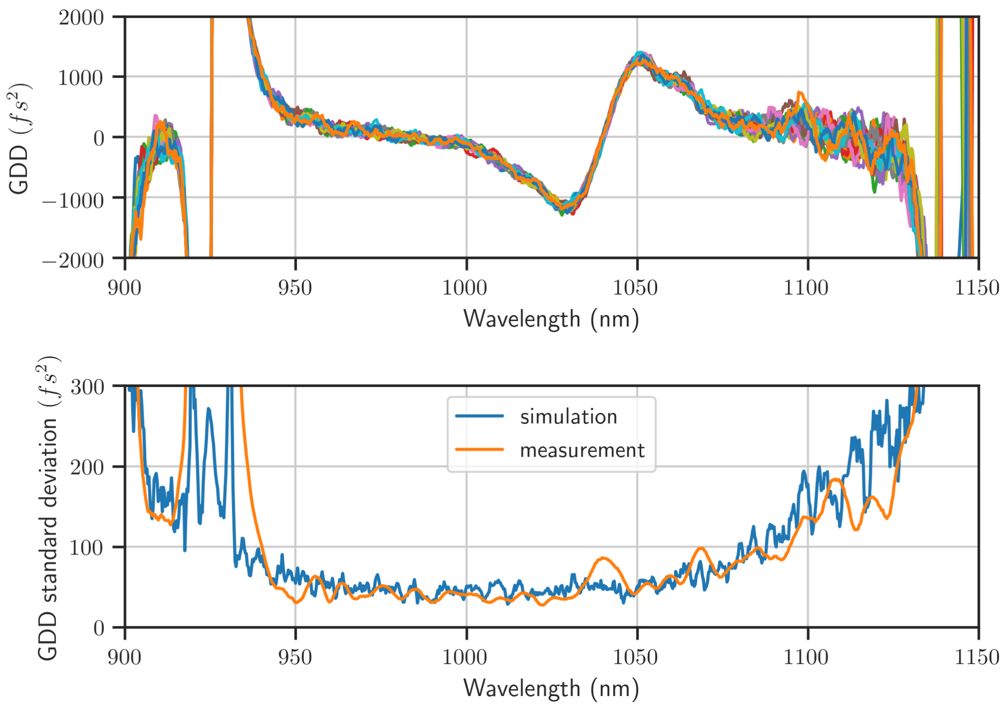

Abbildung 5.13: The upper frame shows a set of GDD curves, based on set of identical interferograms on which an error was added equal to the sum of all error sources. The lower frame compares the GDD error based on the measurements to the simulation results.

In theory, the standard deviation of the mean, also known as standard error, should scale with:

$$\sigma_{mean} = \frac{\sigma}{\sqrt{N}} \tag{5.4}$$

where σ represents the standard deviation of the measurement samples and N the number of samples that have been averaged. This relation is based on the statistical independence of the samples. Meaning, if we can not guarantee that all samples are completely independent of each other then equation 5.4 does not hold in general. Because we can observe some degree correlations in our measurements, i.e. slow color temperature drifts that cause small degrees of correlations, we have to examine if the relation stated above holds.

For that reason we ran a measurement collecting 5000 samples over a time span of ten hours. If equation 5.4 is violated in any situation it is expected to be violated in this measurement.

To test the relation shown in equation 5.4, we performed the following test: The original samples are group together in several bins of equal size and averaged. These averaged samples

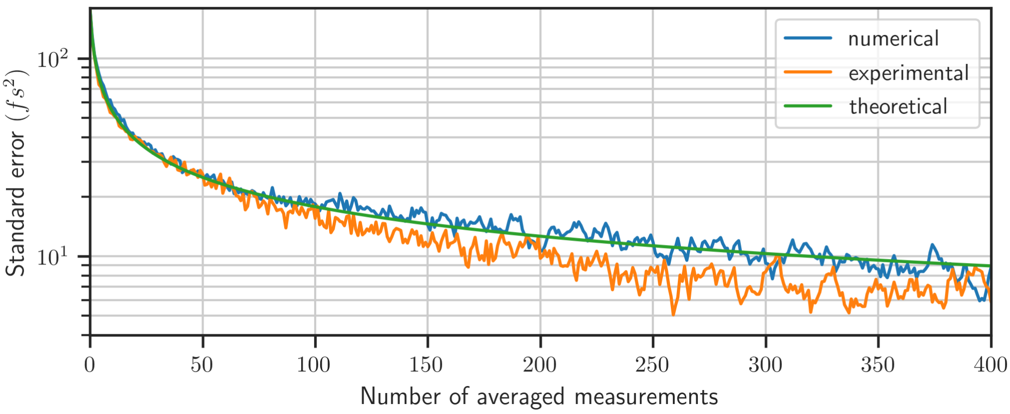

Abbildung 5.14: The standard deviation of set of bins which contain a averages of a certain size are shown. In green the expected trend is shown. The blue graph shows an experiment with artificial data sets, to get an idea of the variations we can expect. In orange we see results of our measurement.

will then be used as a new set of samples. The standard deviation between the sets of averaged samples can be calculated. This standard deviation represents the standard error of the original set. As one might suspect, the standard deviation which is calculated with this method is depended on the bin size. Hence, the standard deviation of bins which contain the average from i.e. 100 measurements is expected to be lower then the one which is only based on bins which contain the average of 10 measurement.

This process is repeated for all a range of possible bin sizes. If equation 5.4 holds, it is expected that the resulting standard deviations are proportional to $1/\sqrt{N}$. The results of this measurements are shown in figure 5.14. One thing to note is that with increasing bin size the total amount of bins decreases rapidly. For example, with a bin size of 1000 samples the standard deviation is calculated based on only five bins. Therefore we limit ourselves to examine the standard deviations only for bin sizes of 400 samples and below to have at least ten bins at all time.

As one can see, the standard deviation follows closely the theoretically expected trend. Therefore, we are able to calculate the resulting standard deviation of the mean by equation 5.4.

6 Open Questions & Outlook

6.1 Discussion

6.1.1 Phase-Spectrum Crosstalk

Our MIR source shows to have several strong features in which the output power fluctuates strongly. This is shown in figure 6.1. In the process of evaluating our measurement results, we found that those features induce significant disturbances in the measured phase difference as shown in figure 6.2.

Up to this point, we were not able to pinpoint these features to a specific reason. Our working theory is that they result from atmospheric absorptions. Assume we have wavelength dependent absorptions in the air through which our light beam traverses during a measurement. These absorptions create phase changes due to Kramer-Kronig relation, which would in turn result in visible disturbances in our measured dispersion. This would explain the presence of cross-talk as shown in figure 6.2.

A possible and simple way to verify this conjecture would be to flood the whole setup with nitrogen. Nitrogen is transparent in the examined spectral region. If the assumption holds, this should remove all spectral features and, if our theory holds, also remove disturbances in the measured dispersion. However, this has not been done because other problems were more pressing at the time. Thus, we can not exclude that these features are created by some other source.

6.1.2 Undecidable Phase Jumps

The algorithm to unwrap phase data is based on the assumption that changes in phase are small in between sample points. To be precise, we assume that all changes in phase are smaller then 2π. For fast changes in phase this assumption might not hold. As a result, it might be undecidable whether there is a phase change of 2π or non at all between two points. This problem was first observed in a measurement of the CMS1003 mirror at approximately 3160 nm, where the stop band of the mirror begins, and which also causes a sharp jump in GDD. In that situation the algorithm breaks down and returns the presence or absence of phase jumps seemingly randomly. This effect is referred to as "bistable"GDD. Approximately half of the data sets are evaluated by the routine as if there is no phase jump. The other half is evaluated as if there is.

A plot of this is shown in fig. 6.3.

When we look at the individual phase data sets, as shown in fig 6.4, we can clearly see the problem. This is not an intrinsic problem of the algorithm. It is simply undecidable from a physical standpoint without prior knowledge. The only option to overcome this problem

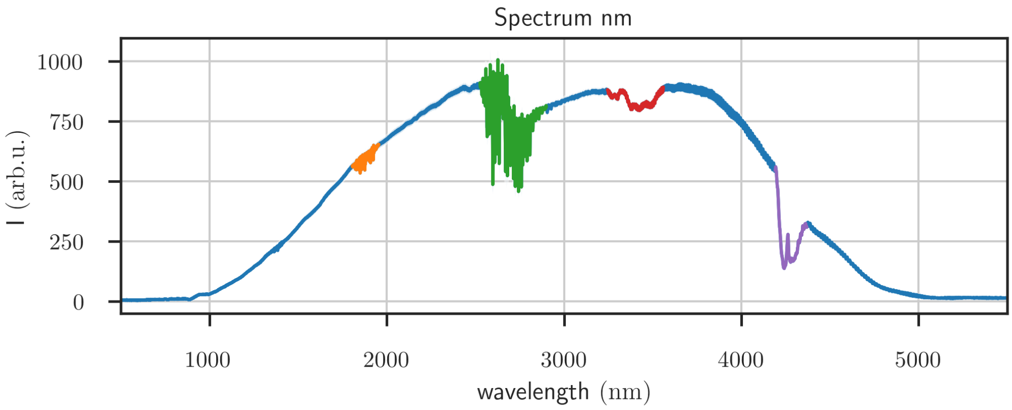

Abbildung 6.1: Output power spectrum of our MIR power source. Several strong features can be seen in the wavelength regions marked in color. The features marked green and orange are absorption lines of water, while the features marked violet are two CO_2 absoption lines.

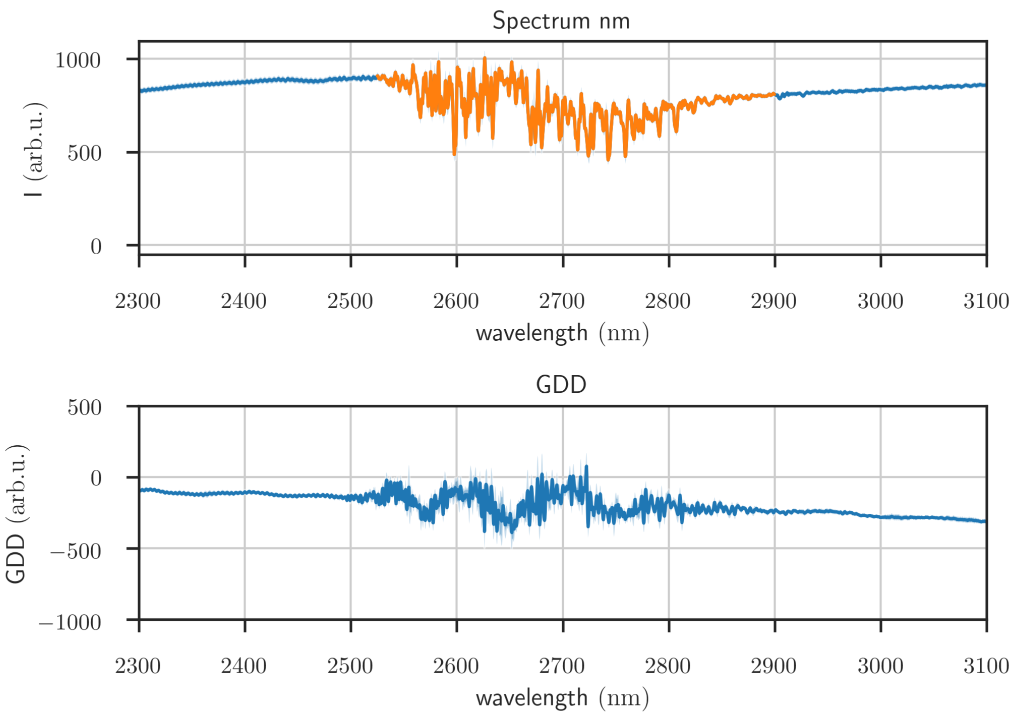

Abbildung 6.2: The presence of spectral features correlates with disturbances in the GDD

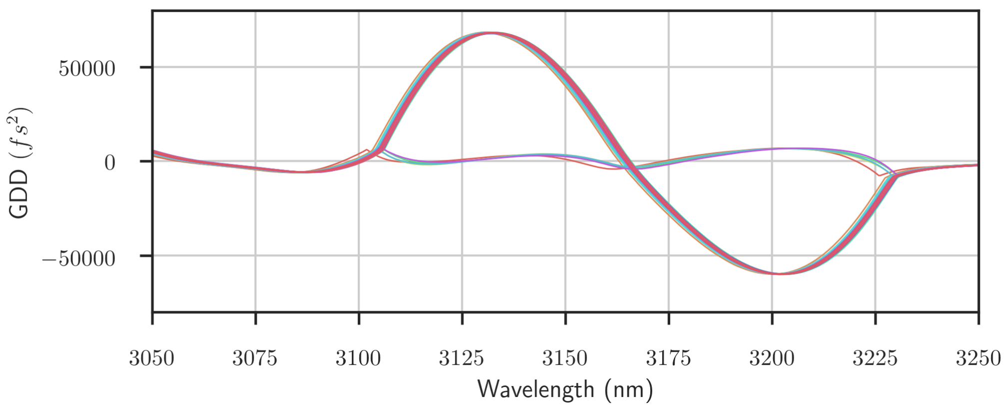

Abbildung 6.3: The resulting GDD from several measurement samples of the same measurement runs are shown. One can clearly distinguish two subsets in the results that show different trends. These occur due to ambiguities in the phase unwrapping process when fast phase changes occur. A sharp feature as shown in figure 6.3 will be smeared over a larger spectral range due to the filtering process. Note that it has been exaggerated for the purpose of demonstration.

without prior knowledge is by increasing the frequency resolution and therefore return in a regime where the previously stated assumption holds.

So far this behavior in phase changes has not been observerd at any other point and thus has not caused any problems as its only occurrence happened outside of an examined stop-band.

6.1.3 Angular Stability of Components

Our measurements are very sensitive to changes in angle between the two interferometer arms. Therefore, we were particularly careful to avoid unnecessary vibrations that might cause changes in angles between the two interferometer arms in the process of designing the setup.

A white frequency spectrum in vibration frequency would cause an additional statistical noise source in our measurement. After minimizing vibrations in the setup, we found the statistical error, that these vibration cause, is negligible. A more crucial topic is a non-white vibration frequency spectrum. If the beam angle is modulated periodically, artifacts in the optical spectrum will appear. This would distort our measurement systematically and therefore introduce a systematic error. During the design and the characterization of the setup, we did not find such critical vibration modes. However, they were not specifically examined, wherefore we can not exclude them. We assume that none of these modes are present, since we neither encountered any nor found any reason to expect that they are present. Nevertheless, they need to be examined if indications arise, suggesting the presence of such modes.

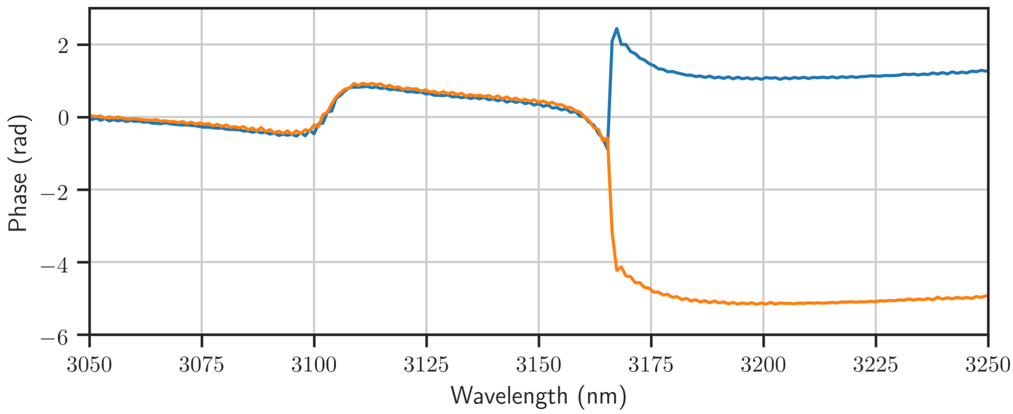

Abbildung 6.4: Both graphs show the unwrapped phase of two measurement samples of the same measurement run. Due to the large phase jump between two sample points, it is undecidable whether a 2Π jump occurred or not during the unwrapping process without prior knowledge.

Regarding angular stability of the setup, another potential problem are slow drifts in the set angle. These would slowly misalign our setup. If the timescale of such a drift is much larger than our measurement time, our measurement would not be effected significantly. However, it would decrease the visibility of the measured interferogram, reducing the measurement precision slowly over time. Such effects could not be found. This reduction in visibility would not cause a systematic but a statistical error. Thus, they would be visible during the evaluation of the measurement.

6.1.4 Detector Linearity

In section 5.1.4 we introduced the difficulties in calibrating an AC-coupled detector regarding its non-linearities in response. Through the AC coupling the total input power at the detector is obscured. However, to be able to compensate for potential non-linearities, we need to know the exact input power as we are trying to compensate non-linear responses to said input power.

Thus, we would be required to always measure the average input power at the detector with an additional, already calibrated detector. This is definitely feasible with i.e. a cw-laser signal with a homogeneous beam profile. The input power of a cw-laser at both detectors can be expected to be proportional to the beam-splitter ratio. However, this task is rather challenging in the case of a white-light interferogram. Slight variations in the detector position relative to the beam result in potential large phase shifts. Therefore, seemingly completely different input powers at the two detectors can be recorded, if the detectors are not perfectly concentric to the interference fringes.

As described in section 6.1.1, we found a cross talk between phase and spectrum. We strongly suspect that these cross-talks are caused by absorption. However, during the process of examining effects of detector linearities, we found that non-linearities in the detector response cause oscillations in spectrum to create oscillations in phase. This, while not suspected, might offer an alternative explanation to the observed phase-spectrum cross-talk.

During our experiments we did not observe any strong linearities. However, non-linearities have been observed during recent work with the same type of detector at another experiment. Because we did not compensate our measurements in any way regarding non-linearities, this might be a potential uncharacterized systematic error. To know if our measurements are affected by this effect, additional experiments need to be performed, as we are currently not able to make any reliable statements regarding the effect on non-linearities on our measurements accuracy.

6.1.5 Output Power

During our measurements with the setup, we permanently found it challenging to make proper use of the rather low output power of our light source. Even though it is collimated to the best of our ability, we end up with a beam spot size of roughly 30 mm at 30 cm distance from the output coupler. To reduce the effect caused by the bad collimation of the light source due to its size, we tried to build the setup as compact as possible. The detected output power could in general be slightly increased by anti-reflection coatings on our optical components. However, these are not an option as the setup is required to perform in a wide spectral range. This has been problem has been improved by replacing the QTH light source with a more powerful GLobar light source. Yet, we found that the power spectral density to be close to the lower minimum.

6.2 Outlook

6.2.1 Noise Reduction

Signal Amplifier

In section 5 we examined all potential noise sources and identified the amplifier as a major noise contributor. The detected output for an average measurement has a voltage level of roughly ± 1 V. The current 12 bit DAQ has a resolution of 5 mV spread over ± 10 V range. This requires us to amplify the signal to make use of the full dynamic range of the DAQ card. Because the discretization error is a larger non-Gaussian error source compared to the other preceding error sources, it is beneficial to use an amplifier. While this is necessary to reduce the influence of discretization error, it also amplifies all preceding errors and it introduces an amplifier as an additional noise source.

With our current DAQ discretization levels of 5 mV, it is beneficial to the measurement accuracy to amplify the signal before capturing it. However, the amplifier could be completely avoided when a higher bit-depth DAQ is used. For example, with 16-bit spreading over the same voltage range, we would reduce the discretization error below 0.5 mV. With this resolution the discretization error is negligible compared to the preceding errors sources. Hence, this would make the amplifier obsolete, which in turn would remove two major error sources at once. This simple improvement is expected to reduce the total noise by over a quarter and is likely the most cost effective improvement.

Amplified and Stabilized Detector

As our detector is currently a major noise contributor, it would be beneficial to improve the detector noise. Yet, this can only be done by replacing it with another detector. We would wish for two properties when replacing our current detector: First of all, we require equal or lower NEP over the same spectral range. Secondly, increasing the band-width would be beneficial to our measurement speed. As described in section 6.2.1 a faster detector can principally be beneficial to the measurement accuracy. This is solely due to the higher amount of averages we could record in the same time.

However, two problems arise with this approach, the first being the cost efficiency. All detector types that satisfied the previous requirements were drastically more expensive. Therefore, it is expected to simply be cheaper to try to improve the setup by other means. The second problem is the temperature stabilization. All fast low noise detectors we found, needed to be temperature controlled. This also requires the detector to be enclosed through some sort of window. Yet, as discussed in section 5.1.2, thin windows cause massive problems in our measurement. Wedging the window in such close proximity of the detector does not avoid the problem of back-reflections as the back-reflected beam still overlaps the original one. Anti-reflection coatings are not available over such a broad spectral range. Therefore, we currently do not know of a detector type which would be more suitable for the application.

Changing Savitzky-Golay Windows

As described in section 3.2, the wavelength resolution scales with λ^2. This results in unequally spaced points on the wavelengths axis. Hence, the size of resolvable features between short wavelengths are much smaller (by a factor of λ^2) than for longer wavelengths. The length of the fitted windows, which are used in the Savitzky-Golay filter, are set to be the same size for all wavelengths. As a result of that, longer wavelengths are fitted over a broader wavelength range. Therefore, broadening effects of the Savitzky-Golay filter are increased for long wavelengths and not, as one could wish for, constant for all wavelengths. To do so, we would need to write a full Savitzky-Golay filter implementation ourselves, since we could not find an openly available implementation that offers the option of varying window widths.

However, to this point, all features that we wished to resolve showed to scale linearly with the frequency. Therefore, they also scaled with a factor of λ^2 regarding the wavelength. For that reason, we did not feel the need to implement such a routine because programming and testing would have taken too much time under these circumstances.

Spectral Resolution Improvements

As shown in section 6.1.2, a higher frequency resolution is not only desirable for resolving spectra and phases better, but also to rid ourselves from undecidable phase jumps. In section 3.2 we showed that the frequency resolution is proportional to the maximal OPD during the capturing of the interferogram.

In the earlier stages of designing the setup, the OPD was limited by the thickness to beam splitter due to unwanted back-reflections. In the current design of the setup we are solely limited by the travel range of the translation stage. Since we are highly susceptible to vibrations while moving the translation stage, we have to avoid stages with gearing. Voice coil translation stages with longer travel ranges exist, which are suitable for our application. Thus, we could further increase our frequency resolution but the resulting longer travel ranges would introduce additional difficulties. One of these difficulties would require us to replace all optical components which are thinner than the OPD of new translation stage. This, in addition with the cost of a new translation stage, would make the upgrade very costly. Because there was no real need to further improve the resolution in the current situation, we did not look into it.

Another potential problem for a larger maximal OPD is the collimation of the light source. Greater delays require longer beam paths, which in return decrease the signal intensity of the delayed arm if the source is not well collimated. This effect creates a non negligible difference in intensity of both interferometer arms depending on the current optical path difference. It does not only introduce statistical errors, but also systematic ones. In general, the larger the delay, the smaller the signal intensity of the interferometer becomes. This increases the effect of error significantly because the noise of several components is independent of the detector output power. Therefore, reducing the signal-to-noise ratio for smaller light intensities, increases statistical errors. Due to the under representation of the interferogram tails, an additional systematic error is introduced.

Nevertheless, we would like to note that it is possible to build a setup with the same design with an higher resolution if needed.

Scanning Speed

In the current realization of the setup, we scan over an OPD with a sample rate of 50 kHz in three seconds time. This results in an oversampling of over a factor of 12. However, the current MIR detector only has a bandwidth of up to 25 kHz, which reduces the oversampling to a factor of 6. Therefore, we should be able to reduce the measurement time by a factor of 6 with the current components. By doing so, we would be required to carefully test the modified measurement scheme. Most importantly, we would have to make sure that no higher frequencies are present in the measured signal to avoid aliasing effects.

This would enable us to capture 1000 interferograms in under ten minutes, resulting in a precision of below 10 fs^2 in the GDD. With this new configuration, we are limited by the MIR detector. If we would wish to improve this further, the next limiting factor is the translation stage which is shown to be effectively limited to a maximal frequency of approximately 10 Hz. This means, that we can improve our measurement speed by an additional factor of 20, if we would be able to sample with a frequency of 500 kHz. Therefore reducing the measurement time of 1000 samples down to just half a minute. However, to do so we would need to find a new MIR detector with the appropriate band-width. This is expected to be difficult for our application.

Wavelength filters

. The coherence length of light is proportional to the wavelength range present in the signal:

$$\tau \propto \frac{\lambda^2}{\Delta\lambda} \tag{6.1}$$

This offers the opportunity to broaden the interference burst by limiting the spectral range of the signal by i.e. optical band-pass filters. Longer interference bursts result in more high quality data points, as the tails have considerably lower signal-to-noise ratios. This approach can be used to increase the measurement precision. Up to this point, this approach has not been tested because suitable filters were not available. Nevertheless, wavelength filters are expected to be beneficial, especially because they are affordable and easy to incorporate into the setup.

7 Results & Summary

7.1 Dispersion Measurement

The setup was build successfully as designed. In the following chapter, we will discuss its functions and application.

The current setup consists of two parts. The VIS to NIR (VIS) part operates in a wavelength range of 500 nm to 1100 nm, while its NIR to MIR (MIR) counterpart operates in a range from 1000 nm up to 5000 nm. Hence, we are able to cover the full range of 500 to 5000 nm. As described in section 3.2, the wavelength resolution scales with λ^2. Therefore, the VIS setup resolution starts at 0.01 nm at 500 nm and decreases quadratically to 0.04 nm at 1100 nm. For the MIR setup we start with a resolution of 0.04 nm at 1100 nm and end up 1 nm at 5000 nm. At an average wavelength of 2500 nm we achieve 0.25 nm resolution.

The standard error on the second order dispersion or GDD is of course depending on several parameters, i.e. the total light power compared to the dynamic range of the detector. For an ordinary measurement we reach a standard error of below 10 fs^2 for both setups calculated for 500 independent measurement runs. As the standard error scales with $1/\sqrt{\mathrm{N}}$, with N being the number of measurements, this standard error can easily be reduced by increasing the amount of averaged measurements. With the recommended improvements to the setup, discussed in section 6.2, we expect to be able to push the standard error of the GDD into the lower single digits fs^2.

Operating the setup was continuously improved, so that at this point it is very easy to operate it without much prior knowledge. A full measurement run takes approximately 5 to 60 minutes with an additional 10 minutes of switching mirrors and realigning the setup. Regarding the measurement speed, the current limiting factors are the DAQ and the MIR detector. In section 6.2 we will present several smaller improvements which increase the measurement precision further.

7.2 Spectrum Measurement

By measuring the interferogram of the Michelson-Interferometer, we can not only extract the phase, but also the spectral intensity of the light transmitted through the interferometer. This is a great feature which was not required by design but is a helpful byproduct of the Fourier-analysis. This feature can be used as a diagnostics tool when measuring dispersion. However, it can also be used as an optical spectrometer analyzer for measuring transmission spectras of components or light sources.

As described in section 3.2 the wavelength resolution is in principal solely limited by the maximal difference in optical path length between the two arms. This makes the setup a very effective tool as its wavelength resolution is at least one nanometer. Because the resolution scales with λ^2, it quickly reduces itself from a resolution of 1 nm at 5 μm wavelength to 0.2 nm at 2.5 μm. Spectral resolution improvements are possible, yet they require a new translation stage with a longer travel range. However, suitable translation stage are rather expensive and grow rapidly in price. Furthermore, longer travel ranges will reintroduce problems with back-refection. This could only be avoided through new optical component which would make this even more difficult. For the dispersion measurement we are required to measure with very high precision. For this reason the statistical error of the spectral power density is found to below approximately 5% in our measurements without any optimization.

In conclusion this setup is able to work as a spectrometer in a range of 500 nm to 5000 nm with an average resolution of 0.2 nm, while the measurements have an approximate standard error below 5% without any optimization. This error scales with $1/\sqrt{\mathrm{N}}$ as well, with N being the number of measurement. Thus, high precisions can be achieved with stable light sources.

8 Appendix

8.1 Code

All code used in the development and application of the setup is publicly available and free for use under the GNU public license version 3 at: `https://bitbucket.org/lsteidle/wli_dispersion/`

Almost all of the code is written in python^{TM} 3, except the application user interface (API) of the DAQ card was only available in C at the time. Frequent use has been made of the NumPy and SciPy packages for python. For python, see `www.python.org`. For Numpy & Scipy, see `www.numpy.org` & `www.scipy.org`

Implementation details of Data evaluation

Reference beam evaluation

Calibrating stage velocity With knowledge of phase changes in the reference laser interferogram, we can compensate for disturbances in the travel velocity of the stage. The compensated phase can be computed by this exemplary python pseudo code snippet:

```
ref_ifft         = fft.ifft(ref)
phase_modulation = unwrap(angle(ref_ifft))
freq_carrier     = 1 / ref.size * index_carrier
phase_carrier    = linspace(N) * 2 * pi * freq_carrier
phase_full       = phase_carrier + phase_modulation
phase_norm       = phase_full * N / phase_full[-1]
# Note: [-1] represents the last value in an array
        linespace()  creates a series of numbers ranging
        from zero to input value
```

Keep in mind that we are talking about the phase of the carrier frequency over time and not about the phase of different frequencies present in the signal.

Calibrating frequency axis The reference signal is also being used to calibrate the frequency/wavelength axis of the Fourier transformed signal. The maximal intensity peak in the Fourier-transformed reference signal is assumed to be the center wavelength of the previously calibrated reference laser. If we identify this frequency bin with our laser frequency, we can calibrate the frequency axis by a linear interpolation. A exemplary implementation in pseudo code is shown below.

```
ref_freq = c / ref_lambda
hz       = linspace(ref.size)
hz_delta = ref_freq / ref_freq_index
hz      *= hz_delta
nm       = c / hz
```

Signal beam evaluation

With the information gained by the evaluation of the reference beam, we are now able to compensate the time axis of our signal for potential variations in OPD changes. This is achieved by interpolating the signal with the phase of reference beam. It is done by a linear interpolation as shown below.

```
signal = interpolate(linspace(signal.size), phase_norm, signal)
```

For our next step we remove common voltage offsets in the signal. This has no real meaning for our evaluation. Nonetheless, it removes a degree of arbitrariness in the data which makes it easier to compare it to other data sets. To remove an arbitrary linear phase term in our signal, which would vanish in the second derivative, we roll the signal in the time domain in such a way that its main intensity peak is at the very beginning of the array. This removes a degree of arbitrariness in the data by setting the phase of the central wavelength to zero.

After being rolled, the signal is Fourier transformed to receive the phase for any resolvable wavelength. The resulting phase has to be unwrapped as described before. At this point, it would principally be sufficient to derive the phase twice to receive the group delay dispersion. However, deriving a discrete signal is by itself a complex subject and is known to amplify errors in the derived data.

8.2 Components

In this section we will list all components used in the setup.

	NIR	MIR
Source	QTH10	SLS203
BS1	BSF2550	WG51050
BS2	BS013	BSW511R
Mirrors	PF10-03	PF10-03
Detector	DET36A	PDA20H
CW-Detector	PDA10A	

Others

- DAQ: Measurement Computing™ USB-201
- Translation Stage: Zaber™ X-DMQ12P-DE52
- Amplifier power supply: DIGILENT 12V PowerBRICK

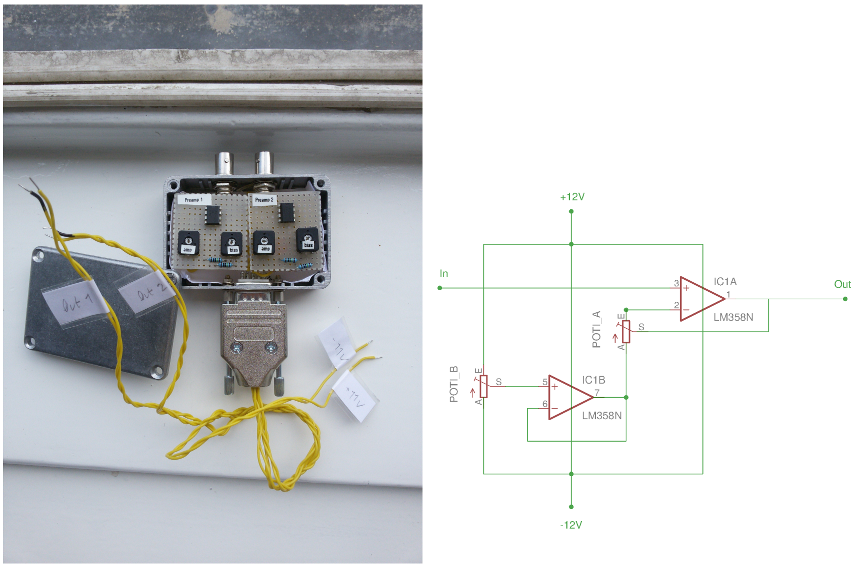

Abbildung 8.1: On the left a picture of the opened amplifier box is shown. On the right a schematic of the circuit used in the amplifier is presented. The amplifiert contains to channels to measure the broad-band and reference signal simultaneously.

Amplifier

The circuit we used for our amplifier is shown in figure 8.1. It is powered by a 12V Power-Block, which is connected to the controlling computer via USB.

Both OpAmps are Texas Instruments LM385. OpAmp B (Labeled as IC1B) is used in combination with potentiometer B to adjust the voltage offset for OpAmp A which determines in combination with potentiometer A the Amplification. OpAmp B works as a voltage follower. Hence, drastically improves the input impedance to the power source and therefore reduces noise and distortions caused by a changing supply voltage.

OpAmp A works as a linear non-inverting amplifier. The Potentiometer have a maximal resistance of $230k\omega$. Their actual size is insignificant as long as they are much bigger then any unwanted resistances in the circuit, i.e. in the wiring. The detector output level might be low compared to noise induced from the environment. Therefore the circuit is shrouded in a simple metal box to reduce electrical noise induced from the environment. A picture of the circuitry is shown in figure 8.1

Literaturverzeichnis

[1] R. K. Shevgaonkar. *Fiber Optics*. 2012.

[2] Scott Diddams and Jean-Claude Diels. Dispersion measurements with white-light interferometry. *J. Opt. Soc. Am. B*, 13(6):1120–1129, 1996.

[3] Mitsuo Takeda, Hideki Ina, and Seiji Kobayashi. Fourier-transform method of fringe-pattern analysis for computer-based topography and interferometry. *Journal of the Optical Society of America*, 72(1):156, 1982.

[4] Abraham Savitzky and Marcel J.E. Golay. Smoothing and Differentiation of Data by Simplified Least Squares Procedures. *Analytical Chemistry*, 36(8):1627–1639, 1964.

[5] Horst Ziegler. Properties of Digital Smoothing Polynomial (Dispo) Filters. *Applied Spectroscopy*, 35(1):88–92, 1981.

[6] Jianwen Luo, Kui Ying, Ping He, and Jing Bai. Properties of Savitzky-Golay digital differentiators. *Digital Signal Processing: A Review Journal*, 15(2):122–136, 2005.

[7] Whitham Reeve. *Noise Concepts*. 2014.

[8] William a. Ling and Audrey K. Ellerbee. The effects of reduced bit depth on optical coherence tomography phase data. *Optics Express*, 20(14):15654, 2012.

[9] F.J. Harris. On the use of windows for harmonic analysis with the discrete Fourier transform. *Proceedings of the IEEE*, 66(1):51–83, 1978.

[10] Tatiana V Amotchkina, Alexander V Tikhonravov, Michael K Trubetskov, Dirk Grupe, Alexander Apolonski, and Vladimir Pervak. Measurement of group delay of dispersive mirrors with white-light interferometer. *Applied optics*, 48(5):949–56, 2009.

[11] Steven W. Smith. Fourier Transform Properties. *Digital Signal Processing*, pages 185–208, 2003.

[12] Gar-Wing Truong, Eleanor M. Waxman, Kevin C. Cossel, Esther Baumann, Andrew Klose, Fabrizio R. Giorgetta, William C. Swann, Nathan R. Newbury, and Ian Coddington. Accurate frequency referencing for fieldable dual-comb spectroscopy. *Optics Express*, 24(26):30495–30504, 2016.

[13] Dallas L. Rabenstein. Sensitivity enhancement by signal averaging in pulsed/Fourier transform NMR spectroscopy. *Journal of Chemical Education*, 61(10):909–913, 1984.